Contrib Mineral Petrol (2003) 145: 515–533
DOI 10.1007/s00410-003-0448-z

ORIGINAL PAPER

Timothy L. Grove · Linda T. Elkins-Tanton
Stephen W. Parman · Nilanjan Chatterjee
Othmar Müntener · Glenn A. Gaetani

Fractional crystallization and mantle-melting controls on calc-alkaline differentiation trends

Received: 1 August 2002 / Accepted: 8 January 2003 / Published online: 21 June 2003

Abstract The phase relations of primitive magnesian andesites and basaltic andesites from the Mt. Shasta region, N California have been determined over a range of pressure and temperature conditions and H_2O contents. The experimental results are used to explore the influence of H_2O and pressure on fractional crystallization and mantle melting behavior in subduction zone environments. At 200-MPa H_2O-saturated conditions the experimentally determined liquid line of descent reproduces the compositional variation found in the Mt. Shasta region lavas. This calc-alkaline differentiation trend begins at the lowest values of FeO*/MgO and the highest SiO_2 contents found in any arc magma system and exhibits only a modest increase in FeO*/MgO with increasing SiO_2. We propose a two-stage process for the origin of these lavas. (1) Extensive hydrous mantle melting produces H_2O-rich (>4.5–6 wt% H_2O) melts that are in equilibrium with a refractory harzburgite (olivine + orthopyroxene) residue. Trace elements and H_2O are contributed from a slab-derived fluid and/or melt. (2) This mantle melt ascends into the overlying crust and undergoes fractional crystallization. Crustal-level differentiation occurs under near-H_2O saturated conditions producing the distinctive high SiO_2 and low FeO*/MgO characteristics of these calc-alkaline andesite and dacite lavas. In a subset of Mt. Shasta region lavas, magnesian pargasitic amphibole provides evidence of high pre-eruptive H_2O contents (>10 wt% H_2O) and lower crustal crystallization pressures (800 MPa). Igneous rocks that possess major and trace element characteristics similar to those of the Mt. Shasta region lavas are found at Adak, Aleutians, Setouchi Belt, Japan, the Mexican Volcanic Belt, Cook Island, Andes and in Archean trondhjemite–tonalite–granodiorite suites (TTG suites). We propose that these magmas also form by hydrous mantle melting.

Introduction

In subduction zone settings, fractional crystallization of primitive magmas derived from the mantle wedge above the subducted oceanic lithosphere is often called upon to produce andesitic lavas that characterize the common eruptive rock type of arc volcanoes (see Gill 1981; Thorpe 1982, for reviews). Alternatively, a subset of subduction zone magmas have been proposed to be direct melts of the subducted oceanic lithosphere. Notable examples of these lavas include the Adak-type high-Mg andesites from the Aleutians (Kay 1978; Yogodzinski et al. 1995) and the Setouchi high-Mg andesites from SW Japan (Tatsumi and Ishizaka 1982; Ishizaka and Carlson 1983; Shimoda et al. 1998). These lavas are found in subduction zone environments where the age of the subducted oceanic crust is young. The lavas of the Mt. Shasta region provide an unparalleled opportunity to examine the processes of subduction zone magma generation in a young, hot-slab environment. Mt. Shasta lies above the young (12–14 million years old) subducting Juan de Fuca plate (Wilson 1988; Green and Harry 1999) and, therefore, represents an environment of hot oceanic lithosphere subduction. Partial melting of mantle wedge peridotite fluxed by volatiles from the subducted oceanic lithosphere has played an important role in the origin of Mt. Shasta region primitive lavas. In this paper, we present experimental evidence relevant to the conditions of mantle melting and crustal level

---

T. L. Grove (✉) · L. T. Elkins-Tanton · S. W. Parman
N. Chatterjee
Department of Earth, Atmospheric and Planetary Sciences,
Massachusetts Institute of Technology, Cambridge, MA 02139,
USA
E-mail: tlgrove@mit.edu

O. Müntener
Institut de Géologie, Université de Neuchâtel, Neuchâtel,
Switzerland

G. A. Gaetani
Department of Geology and Geophysics,
Woods Hole Oceanographic Institution, Woods Hole,
MA 02543, USA

Editorial responsibility: J. Hoefs

fractional crystallization experienced by Mt. Shasta region lavas. We will demonstrate that the major element characteristics of these lavas are controlled by a hydrous mantle melting process that has extended to shallow mantle depths.

The model developed in this paper (Fig. 1) explores a melting process that is initiated when H_2O is released from subducted oceanic lithosphere by dehydration of hydrous minerals and/or vapor-saturated anatexis (I, Fig. 1). This H_2O-rich component rises into the overlying mantle, interacts chemically with mantle peridotite (II, Fig. 1, Zhang and Frantz 2000), and ultimately vapor-saturated mantle melting takes place near the base of the wedge (III, Fig. 1). This vapor-saturated melt segregates from its residue and ascends to shallower mantle depths where it encounters progressively higher mantle temperatures. Melting progresses by a reactive porous flow process (flux melting). As the melt traverses the inverted thermal gradient in the mantle wedge and encounters hotter, shallower mantle, it finds itself out of equilibrium with its surroundings. In order to equilibrate with the surrounding peridotite, the temperature of the melt increases and the melt dissolves silicate minerals, resulting in a decrease in melt H_2O content as equilibration pressure decreases. This process continues to shallow mantle depths where a hydrous melt is segregated (IV, Fig. 1). This flux-melting model (Grove et al. 2002; Gaetani and Grove 2003) results in a dilution of the slab-contributed trace element and fluid components through significant (> 20 wt%) melting of the mantle. By the time it has reacted its way to the top of the mantle wedge, the melt is far from vapor saturation. This H_2O-undersaturated mantle melt passes into the crust and ultimately undergoes fractional crystallization (and other crustal interaction processes) in shallow magma reservoirs (V, Fig. 1). Under low-pressure conditions the H_2O content of the melt is sufficiently high that crystallization takes place at near vapor-saturated conditions (200 MPa). The focus of this paper is the establishment of the depth and H_2O contents of the mantle melt at step IV, and the modification of that melt during step V.

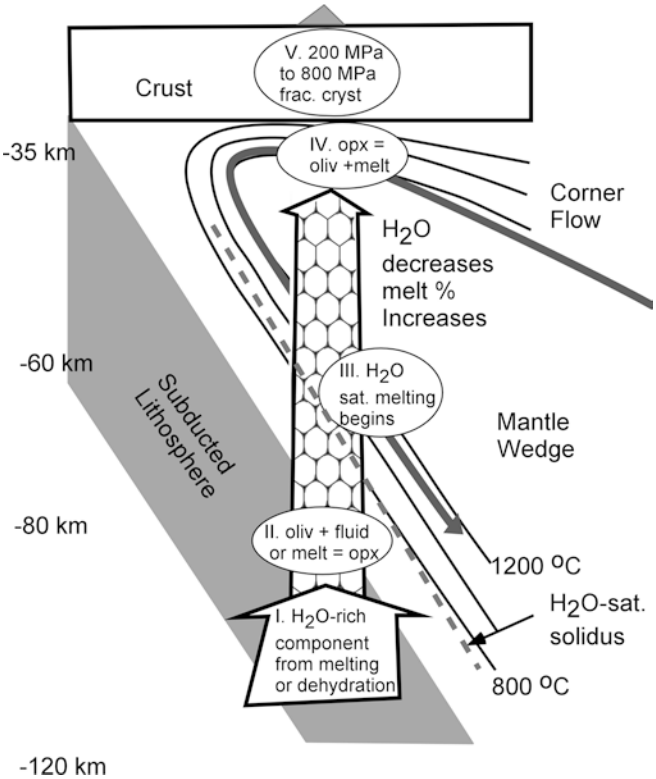

Fig. 1 Model of melt generation and subsequent modification of hydrous magmas produced in the mantle wedge. An H_2O-rich component is derived by dehydration of minerals in the subducted lithosphere and/or by low-degree vapor saturated melting of subducted sediment or basalt (*I*). This H_2O-rich component ascends into the overlying mantle wedge, where it is modified by reaction with the descending mantle and SiO_2 is stripped from the fluid-rich component (*II*). The modified fluid-rich component ascends into shallower, hotter mantle that exceeds the vapor-saturated solidus of peridotite and melting begins (*III*). Melting takes place throughout the mantle wedge by reactive porous flow (Grove et al. 2002; Gaetani and Grove 2003) and continues into the shallow part of the mantle wedge, where the melt becomes SiO_2-rich by dissolving opx and precipitating oliv (**IV**). Finally the magma reaches the overlying crust where assimilation of deep and shallow crust, fractional crystallization and magma mixing operate to modify most subduction zone magmas (*V*)

Experimental methods

Starting materials

Synthesis experiments were performed using two of the most primitive lavas from the Mt. Shasta region, northern California, USA, a basaltic andesite (85-44) and a primitive magnesian andesite (85-41c). Compositions of the starting materials are reported in Table 1. The bulk composition of basaltic andesite 85-44 is in equilibrium with the most magnesian olivine present in the lava ($Fo_{89.6}$, Baker et al. 1994). Sample 85-41c contains $Fo_{93.6}$ olivine, but has experienced a small amount of contamination by a SiO_2-rich liquid (Anderson 1974, 1979; Baker et al. 1994). When the bulk composition is corrected for contamination and brought into equilibrium with the $Fo_{93.6}$ olivine (oliv), the resulting composition has ~55 wt% SiO_2. Composition A was calculated as an analog to 85-41c to represent a melt in equilibrium with the Fo_{90} oliv, and this composition (A) was also used for experiments (Table 1). Both 85-44 and 85-41c have been used in experimental studies by Baker et al. (1994) and Müntener et al (2001).

Experimental procedures

Three starting materials were used: natural powders of 85-44 and 85-41c and an H_2O-bearing oxide mix similar to 85-41c (Composition A). Samples 85-44 and 85-41c were reduced to powders by grinding in a SPEX shatterbox for 3 min, and then subjected to grinding in an agate mortar and pestle for an additional 15 min under ethanol. Composition A was prepared from a mix of high purity oxides (Gaetani and Grove 1998). Composition A was conditioned by melting it in a gas pressure vessel at 200 MPa, H_2O-saturated conditions. This produced a starting composition with 4.5 wt% H_2O, and this material was powdered in an agate mortar and used as the starting mix. Experiments were carried out under a variety of conditions with respect to H_2O content: dry at 0.1 MPa and 1 GPa, H_2O-saturated at 200 and 800 MPa, and H_2O-undersaturated at 1 to 1.3 GPa.

Table 1 Compositions of Mt. Shasta region lavas used as starting materials in this study and other compositions used in H_2O-saturated melting experiments of subduction zone magmas

Sample	SiO_2	TiO_2	Al_2O_3	FeO	MnO	MgO	CaO	Na_2O	K_2O	P_2O_5	Sum	Mg#
85-41c[a]	57.79	0.60	14.46	5.74	0.11	9.14	8.17	3.11	0.71	0.15	100.0	0.74
85-44[a]	51.68	0.60	16.40	7.93	0.16	10.79	9.67	2.24	0.42	0.11	100.0	0.71
A[a]	57.03	0.56	14.16	7.20	0.07	9.16	8.02	3.00	0.69	0.11	100.0	0.70
79-35g[b]	48.2	0.66	18.2	8.39	0.16	9.86	12.0	2.29	0.09	0.05	99.9	0.68
82-66[b]	51.2	1.01	17.3	8.66	0.16	7.47	10.2	3.11	0.70	0.16	100.0	0.61
87S35[b]	51.12	1.28	19.3	8.78	0.17	4.36	8.94	4.27	1.01	0.37	99.6	0.47
1140Mf[c]	56.3	0.95	17.4	7.17	0.12	4.42	7.88	3.54	1.26	0.18	99.2	0.47
1471Mb[d]	52.1	1.13	17.9	9.03	0.16	5.98	9.70	3.44	0.48	0.18	100.7	0.54
Mas-22[e]	55.83	0.75	17.59	6.05		6.75	7.36	4.01	1.19	0.27	99.8	0.67
MAS-911[f]	59.28	0.91	14.8	4.82	0.08	6.64	7.40	3.83	1.77	0.19	99.7	0.71

[a] Analyses reported in Baker et al. (1994) and Grove et al. (2002). Primitive magnesian andesite corrected for crustal contamination and calculated to be in equilibrium with Fo_{90} olivine

[b] Medicine Lake basalts and Sierra Nevada mafic dikes investigated by Sisson and Grove (1993a)

[c] Medicine Lake basalts and Sierra Nevada mafic dikes investigated by Grove et al. (1997)

[d] Medicine Lake basalts and Sierra Nevada mafic dikes investigated by Wagner et al. (1995)

[e] Basaltic andesite from the western Mexican volcanic belt (Moore and Carmichael 1998)

[f] Andesite from the western Mexican volcanic belt (Blatter and Carmichael 1998)

Synthesis experiments at 0.1 MPa were performed on 85-41c in Deltech DT31-VT rapid-quench gas mixing furnaces. Experiments were performed at the quartz–fayalite–magnetite (QFM) buffer using CO_2–H_2 gas mixtures at flow rates of 0.1 ml/s or less. Experimental methods were similar to those described in Tormey et al. (1987) with the following exceptions. Pellets of starting material (0.07–0.09 g) were pressed using elvanol as a binder, and sintered to 0.008″ FePt alloy loops preconditioned to minimize Fe exchange between the silicate sample and the loop (Grove 1981). Oxygen fugacity was monitored using CaO–ZrO_2 electrolyte cells calibrated at the Fe–FeO, Ni–NiO, and Cu–Cu_2O buffers. Temperature was monitored using Pt-10Rh thermocouples calibrated against the melting points of NaCl, Au, and Pd on the IPTS 1968 temperature scale.

Synthesis experiments were carried out at 200 MPa on both 85-44 and 85-41c under H_2O-saturated conditions in ZHM (Zirconium-Hafnium carbide-Molybdenum) cold seal pressure vessels following experimental procedures described in Sisson and Grove (1993a, 1993b) with the following exceptions. Experiments performed at temperatures < 1,050 °C used Au inner and outer capsules while experiments performed above 1,050 °C used $Au_{90}Pd10$ alloy inner and outer capsules. Oxygen fugacity was controlled at the nickel–nickel oxide (NNO) buffer. The buffer assemblage was isolated from contact with the Au by placing it into two or three unsealed Pt capsules. Temperature measurement, calibration, pressure application, and gas mixtures are as described in Sisson and Grove (1993a, 1993b). The pressure vessel was positioned vertically in a Deltech DT31VT furnace and held at pressure and temperature of the experiment for its duration. Experiments were terminated by removing the vessel from the furnace, inverting it and rapping on the hot portion of the vessel with a wrench. The capsule dropped to the water-cooled pressure seal and quenched rapidly with no growth of quench crystals.

Synthesis experiments at 800 MPa were carried out on 85-44 under H_2O-saturated conditions in a 0.5″ solid medium piston cylinder apparatus (Boyd and England 1960). Experiments were pressurized to 800 MPa at room temperature, and then the temperature was raised to 865 °C at 100 °C/min. The experiment was held at these conditions for 6 min, and then the temperature was raised to the final run conditions at 50 °C/min. The sample was held at isothermal conditions for the duration of the experiment (Table 2). At the end of the experiment, the sample was quenched by turning off the power. The pressure medium was $BaCO_3$, and pressure was calibrated against the reaction: anorthite + gehlenite + corundum = Ca-tschermakite (Hays 1966). Pressures are thought to be accurate to ± 50 MPa. Temperature was monitored and controlled using $W_{97}Re3$–$W_{75}Re25$ thermocouples with no correction applied for the effect of pressure on thermocouple EMF. The sample was placed in the center of the furnace, and a correction of 20 °C was applied to account for the temperature difference between the thermocouple and the hot spot. This temperature difference was measured using offset thermocouples. Temperatures are thought to be accurate to ± 10 °C.

A modified two-capsule technique similar to that used for the ZHM experiments at 200 MPa was developed to achieve H_2O-saturation and oxygen buffering in the piston cylinder at 800 MPa. A shorter outer Au capsule (~0.75″) was triple crimped on the bottom, welded, and flattened by hammering with a drill blank. An inner Au capsule containing the silicate starting material was loaded into the outer capsule along with two Pt capsules containing the Ni–NiO buffer. These capsules were welded on one end and crimped on the other. A micro-syringe was used to add ~15–20 µl H_2O and the outer capsule was crimped flat and welded shut.

After termination of the 200 and 800 MPa H_2O-saturated experiments by quenching, the outer capsules were punctured to verify the presence of water. The buffer capsules were examined for the presence of both Ni and NiO, and to verify that there was no leakage of silicate material into the buffer capsules. Experiments that passed both of these tests were considered successful and were mounted for analysis by electron microprobe. Experimental temperatures and durations are reported in Table 2 and chemical analyses of experimental products are presented in Table 3.

Anhydrous and H_2O-undersaturated experiments on composition A were carried out in a piston cylinder apparatus. Anhydrous experiments used oxide mix samples packed into a graphite capsule that was then placed in a Pt capsule and welded shut. H_2O-bearing sample powders of composition A (4.5 wt% H_2O) were used for H_2O-undersaturated melting experiments. These powders were placed in an $Au_{80}Pd_{20}$-Fe alloy capsule and welded shut. The capsules were placed inside graphite capsule machined from graphite rod. The experimental setup is essentially the same as developed by Gaetani and Grove (1998). The $Au_{80}Pd_{20}$ capsules were pre-conditioned with Fe before the high-pressure experiments. This was done by filling them with an andesite composition and placing them in a 1-atm furnace at $\log f_{O2} = \text{QFM-1}$ and 1,250 °C for 72 h. The silicate glass was then removed using HF + HNO_3. Fluoride residues after HF dissolution were first removed manually with a pick and then by soaking in HCl. Experimental conditions are given in Table 2 and compositions are reported in Table 3.

Experimental durations varied widely depending on limitations imposed by the experimental geometry and the time duration inferred from previous experimental studies required for establishment of exchange equilibrium. In the 0.1-MPa experiments the duration varied from 40 h at near liquidus conditions to 230 h at high degrees of crystallinity. These durations were based on the time that Grove and Juster (1989) found necessary for establishment

Table 2 Experimental conditions and products. Experiments at 0.1 MPa were buffered at QFM using CO_2–H_2 gas mixing. Experiments on 85-41c and 85-44 at 200 and 800 MPa were buffered at NNO with $P_{H2O} = P_{total}$. Experiments on composition A are H_2O-undersaturated and contain 0 or 4.5 wt% H_2O added. See Table 3 for phase compositions

Run no.	T (°C)	P (MPa)	Time (h)	Phases[a]	ΣR^2	% Fe loss[b]	K_D ol/liq	K_D pl/liq	K_D cpx/liq	K_D opx/liq	K_D amp/liq
85-41c											
#1	1,250	0.1	44	gl (100), ol (< 1)	0.86	12.0	0.266				
#2	1,225	0.1	44	gl (98), ol (3), sp (-1)	0.56	5.6	0.289				
#3	1,200	0.1	53	gl (89), ol (-3), opx (16), pl (-2)	0.07	< 1	0.272	1.27		0.256	
#4	1,175	0.1	40	gl (90), ol (-4), opx (14), sp (< 1)	0.76	12.0	0.247			0.196	
#8	1,160	0.1	174	gl (57), cpx (5), opx (18), pl (20)	0.69	−4.8		1.29	0.250	0.256	
#5	1,150	0.1	50	gl (63), cpx (6), opx (16), pl (15)	0.02	< 1		1.57	0.233	0.210	
#6	1,125	0.1	86	gl (40), cpx (11), opx (20), pl (29)	0.13	3.5		1.80	0.203	0.203	
#7	1,120	0.1	230	gl (44), cpx (9), opx (20), pl (27)	0.15	2.3		1.71	0.219	0.222	
#5	1,040	200	26	gl (82), ol (8), cpx (10)	0.21	−7.2	0.275		0.247		
#7	1,020	200	44	gl (75), ol (12), cpx (15), opx (-2), sp (< 1)	0.02	< 1	0.293		0.244	0.281	
#8	980	200	50	gl (46), cpx (15), opx (19), pl (20), sp	0.11	-4.6		2.34	0.216	0.284	
#9	940	200	48	gl (40), cpx (16), opx (21), pl (24), sp	0.16	1.9		2.83	0.221	0.272	
85-44											
#7	1,090	200	16	gl (96), ol (3), cpx (1)	0.31	< 1	0.291		0.249		
#6	1,070	200	32	gl (77), ol (4), cpx (19), sp (< 1)	0.13	1.5	0.309				
#3	1,030	200	25	gl (55), ol (17), cpx (10), sp (< 1), pl (18)	0.29	< 1	0.298	4.03	0.246		
#4	1,010	200	19	gl (47), ol (18), cpx (13), sp (< 1), pl (23)	0.26	< 1	0.328	4.42	0.250		
#5	990	200	48	gl (41), ol (-5), cpx (28), pl (21), amp (16), sp (< 1)	0.30	< 1	0.292	5.55	0.223		0.297
B372	1,090	800	25	gl, ol							
B375	1,077	800	19	gl, ol, cpx							
B373	1,065	800	21	gl (52), amph (62),opx (-3), cpx (-9)	0.28	4.8			0.284	0.332	0.340
B380	1,045	800	19	gl (47), amph (52), cpx (1), sp (2)	0.24	3.1			0.252		0.313
A				wt. % H_2O added + Phases							
A1.2	1,300	1,500	70	0.0 gl (77), opx (9), cpx (14)	0.62	−1.1			0.33	0.35	
A1.7	1,175	1,000	30	4.5 gl, ol							
A1.8	1,200	1,300	21	4.5 gl, opx, cpx							
A1.9	1,200	1,150	24	4.5 gl, opx, cpx							
A1.10	1,175	1,000	15	4.5 gl, opx, cpx							

[a] Phase proportions calculated by mass balance, ignoring MnO and P_2O_5. Abbreviations for phases are in Table 3

[b] Apparent loss or gain of FeO estimated as $100^*(FeO_{calc}–FeO_{starting\ material})/FeO_{starting\ material}$

of exchange equilibrium between crystals and melt for major elements. At 200 and 800 MPa experiment duration is limited by the rate of hydrogen diffusion through the Au outer capsule. Experiments at 1,070 and 1,090 °C could be continued for ~24 h. At temperatures below 1,000 °C durations of 48 h were possible.

Analytical methods

Compositions of minerals and quenched glasses in the experimental products were obtained with the MIT five-spectrometer JEOL 733 Superprobe using on-line data reduction. For the 200- and 800-MPa experiments analyses were made with automation software that used the matrix correction procedures of Bence and Albee (1968) with modifications of Albee and Ray (1970). For the 0.1-MPa and 1–1.3-GPa experiments on 85-41c newer automation software was employed that utilized the CITZAF correction package of Armstrong (1995). The atomic number correction of Duncumb and Reed, Heinrich's tabulation of absorption coefficients, and the fluorescence correction of Reed were used to obtain a quantitative analysis (Armstrong 1995). A comparison of the two techniques on a basalt standard glass showed no appreciable difference between the results obtained by the two methods. Analyses of mineral and quenched liquid products are presented in Table 3. All analyses were performed using a 15-kV accelerating voltage and a 10-nA beam current. For the glass phase, the beam size was ~20 μm and Na was counted at the beginning of the analysis for 5 s. Other elements were measured for up to 40 s, depending on abundance level. Analytical precision can be inferred from replicate analyses of an andesite glass working standard (38b-129) from a 0.1-MPa experiment (Grove and Juster 1989). One standard deviation of replicate glass analyses expressed as relative percent of oxides are SiO_2:0.4%, Al_2O_3:0.9%, CaO:1.5%, MgO:1.5%, FeO:1.4%, MnO:8.1%, P_2O_5:5%, Na_2O:1.9%, K_2O:1.1%, based on 289 individual measurements over 28 analytical sessions. The mean sum of analyses of the anhydrous glass is 99.4%. Analytical precision for NiO analyses in olivine in Table 3 are poor, but are presented as an indication of the absence of contamination of the silicate sample by the buffer.

Experimental results

Approach to equilibrium

The experiments presented here are all synthesis experiments where crystals and melt have grown from starting materials that consist of a powdered volcanic rock or a melted oxide mix. Phase appearance temperatures have not been reversed because past experience (Grove and Bence 1977) indicates that direct synthesis is sufficient to recover equilibrium appearance temperature when significant (>40 wt%) melt is present. For the reasons outlined below, we conclude that the experiments approached equilibrium sufficiently so that they can be used to understand crystallization behavior under the conditions of this investigation. Maintenance of constant sample composition with little or no loss or gain of iron is an important prerequisite for an approach to equilibrium. A materials-balance technique (Bryan et al. 1969) was used to estimate phase proportions in the experimental products and to estimate iron loss or gain from the starting material. Results are summarized in Table 2, and the loss or gain of iron is considered to be acceptably low, generally less than ± 5 wt% relative. Two exceptions are the 0.1 MPa experiments at 1,250 and 1,175 °C experiments that gained iron from the FePt alloy loop. We include these experiments despite the iron gain because they provide useful information of the low-pressure liquidus phase relations. The reason for the iron gain is that the loops used for these experiments contained more Fe in the alloy than the desired equilibrium amount (7–9 wt%) and this was transferred to the silicate portion of the charge.

Another important criterion for equilibrium is the achievement of regular and consistent partitioning of major elements between crystalline phases and melt. The mineral–melt Fe–Mg exchange distribution coefficient (K_D^{Fe-Mg}) between olivine (oliv) and melt and pyroxene and melt are constant within each bulk composition. For 85-44, the oliv–melt Fe–Mg exchange distribution coefficients ($K_D^{Fe-Mg} = [X_{Fe}^{Ol} X_{Mg}^{Liq}]/[X_{Mg}^{Ol} X_{Fe}^{Liq}]$) have an average value of 0.30 (± 0.02 at 2σ) for the 200-MPa experimental pairs. For 85-41c, the oliv–melt Fe–Mg exchange distribution coefficients the average value is 0.27 (± 0.04 at 2σ) for the 200-MPa experimental pairs. Even though these averages are within 2σ of each other there appears to be a systematic difference in the oliv–melt K_D^{Fe-Mg}, possibly related to the higher SiO_2 content of 85-41c. The high-Ca pyroxene (cpx) K_D^{Fe-Mg} is 0.24 (± 0.02 at 2σ) for the 85-44 and 85-41c pyroxenes and the orthopyroxene (opx)–melt $K_D^{Fe-Mg} =$ 0.24(± 0.04 at 2σ) for the eight opx-bearing experiments in 85-41c. The average of the three amphibole (amph)–melt K_D^{Fe-Mg} values from the 200- and 800-MPa experiments on 85-44 has a value of 0.32 (± 0.04 at 2σ). In composition 85-41c, the plagioclase (plag)–melt Ca–Na exchange distribution coefficient ($K_D^{Ca-Na} = [X_{Ca}^{Pl} X_{Na}^{Liq}]/[X_{Na}^{Pl} X_{Ca}^{Liq}]$) for the 0.1-MPa experiments is 1.6 (± 0.1 at 2σ) and the two plag-saturated 200 MPa experiments give a $K_D^{Ca-Na} =$ 2.6. In the basaltic andesite (85-44), the 200-MPa hydrous plag–melt K_D^{Ca-Na} for the three plag–melt pairs is 4.0 (± 0.1 at 2σ).

The values for the exchange K_Ds and their variations provide an indication of the extent to which a mineral has established Fe–Mg or Ca–Na exchange equilibrium with its enclosing melt. Olivine–melt, cpx–melt, and opx–melt pairs show a regular and nearly constant value for K_D. Plagioclase–melt K_D^{Ca-Na} at 200 MPa is similar to the values found by Gaetani et al. (1994) for Lau Basin basaltic andesite, and lower than the value of 5.5 determined by Sisson and Grove (1993a) for basaltic melts and Moore and Carmichael (1998) for a Mexican volcanic belt basaltic andesite. These values and variations are generally similar to those achieved in experiments of much longer duration where Fe–Mg and Ca–Na exchange reactions have been reversed (Grove and Juster 1989) and are taken to indicate a sufficiently close approach to equilibrium.

Mineral appearances

Basaltic andesite 85-44

The phase appearance sequence for the primitive basaltic andesite is summarized in Fig. 2. At 0.1 MPa,

Table 3 Electron microprobe analyses of phases produced in experiments

Run no.	Phase[a]	SiO_2	TiO_2	Al_2O_3	Cr_2O_3	FeO	MnO	MgO	CaO	Na_2O	K_20	P_2O_5	NiO	Total
85-41c	**0.1 MPa**													
85-41c#1														
	gl (9)[b]	56.5 (3)[c]	0.68 (2)	14.8 (1)	0.08 (1)	6.31 (9)	0.08 (2)	9.01 (8)	7.98 (8)	3.08 (6)	0.69 (2)	0.09 (3)		99.28
	ol (4)	40.9 (9)		0.05 (2)	0.03 (4)	9.45 (12)	0.16 (2)	50.7 (7)	0.23 (2)				0.29 (1)	101.81
85-41c#2														
	gl (7)	57.0 (7)	0.74 (4)	15.4 (1)	0.07 (1)	5.91 (8)	0.07 (2)	7.78 (9)	8.23 (12)	3.30 (8)	0.73 (3)	0.15 (3)		99.34
	ol (4)	40.1 (7)	0.02 (2)	0.05 (1)	0.15 (7)	10.7 (2)	0.15 (1)	48.6 (5)	0.26 (2)				0.13 (3)	100.16
	sp (3)	0.15 (26)	0.33 (6)	21.0 (2)	46.6 (3)	15.5 (4)	0.03 (3)	15.7 (1)	0.18 (5)					99.49
85-41c#3														
	gl (10)	56.7 (3)	0.74 (3)	16.4 (6)	0.04 (2)	5.51 (9)	0.06 (2)	6.22 (8)	8.73 (10)	3.65 (11)	0.79 (4)	0.15 (3)		99.00
	ol (5)	40.4 (5)		0.11 (6)	0.10 (9)	11.6 (2)	0.17 (2)	48.0 (7)	0.29 (5)				0.15 (2)	100.82
	pl (7)	53.7 (7)		28.9 (5)		0.54 (3)		0.34 (4)	12.2 (4)	4.02 (25)	0.15 (1)			99.85
	opx (4)	56.5 (8)	0.11 (2)	1.11 (25)	0.48 (12)	7.31 (50)	0.15 (2)	32.2 (2)	2.02 (19)					99.88
85-41c#4														
	gl (10)	56.8 (2))	0.93 (3)	15.6 (1)	0.06 (1)	6.71 (8)	0.07 (2)	6.89 (5)	8.48 (10)	3.33 (10)	0.73 (3)	0.15 (3)		99.69
	ol (5)	39.4 (6)	0.02 (2)	0.05 (2)	0.03 (7)	11.5 (2)	0.17 (1)	47.8 (7)	0.28 (3)				0.18 (2)	99.43
	opx (4)	56.4 (3)	0.09 (2)	1.18 (18)	0.61 (22)	6.26 (67)	0.13 (2)	32.8 (5)	1.68 (22)					99.15
	sp (4)	0.18 (37)	0.43 (5)	18.1 (9)	48.2 (9)	17.8 (9)	0.10 (3)	14.1 (4)	0.10 (5)					99.01
85-41c#5														
	gl (8)	58.7 (7)	1.01 (4)	15.5 (2)	0.03 (1)	6.16 (7)	0.06 (2)	4.63 (23)	7.60 (10)	3.93 (16)	1.11 (4)	0.23 (3)		98.97
	cpx (10)	53.5 (5)	0.38 (7)	2.21 (47)	0.60 (28)	5.89 (49)	0.14 (2)	19.0 (4)	18.9 (5)	0.19 (7)				100.81
	opx (8)	56.1 (5)	0.16 (3)	1.25 (44)	0.20 (5)	8.70 (67)	0.19 (2)	31.2 (8)	2.24 (17)					100.04
	pl (10)	54.6 (6)		28.7 (5)		0.74 (19)		0.39 (16)	12.1 (3)	3.98 (23)	0.17 (3)			100.68
85-41c#6														
	gl (6)	63.0 (3)	1.33 (9)	14.8 (2)		6.21 (45)	0.06 (2)	3.12 (10)	6.03 (12)	4.02 (9)	1.60 (5)	0.33 (4)		100.49
	cpx (8)	53.2 (3)	0.50 (16)	2.16 (30)	0.23 (12)	7.56 (57)	0.22 (1)	18.7 (6)	17.6 (7)	0.12 (6)				100.29
	opx (8)	55.8 (2)	0.21 (4)	0.96 (40)	0.16 (5)	11.7 (12)	0.24 (4)	29.0 (8)	2.40 (31)	0.03 (2)				100.5
	pl (7)	55.0 (4)		28.7 (5)		1.14 (31)		0.18 (11)	11.4 (4)	4.24 (27)	0.20 (3)			100.86
85-41c#7														
	gl (17)	63.1 (3)	1.16 (4)	14.5 (1)		5.98 (15)	0.11 (2)	3.49 (4)	6.55 (16)	3.80 (20)	1.47 (4)	0.37 (2)	0.05 (2)	100.65
	cpx (5)	53.4 (3)	0.49 (16)	1.66 (16)	0.47 (13)	7.34 (21)	0.19 (3)	19.6 (5)	17.5 (6)	0.11 (8)				100.76
	opx (6)	55.3 (6)	0.22 (6)	1.27 (51)	0.17 (7)	11.2 (4)	0.22 (3)	29.4 (4)	2.29 (26)	0.02 (2)				100.09
	pl (5)	54.4 (3)		28.4 (3)		0.60 (4)		0.40 (2)	12.0 (2)	4.07 (15)	0.18 (2)			100.05
85-41c#8														
	gl (24)	60.0 (4)	0.93 (2)	14.9 (1)		5.77 (15)	0.10 (2)	4.66 (8)	7.80 (12)	3.43 (11)	2.34 (6)	0.25 (3)		100.18
	cpx (7)	53.4 (4)	0.34 (6)	1.95 (38)	0.46 (11)	5.95 (69)	0.17 (2)	19.2 (7)	18.3 (8)	0.12 (3)				99.89
	opx (7)	56.2 (4)	0.16 (5)	1.14 (26)	0.21 (10)	9.74 (64)	0.21 (4)	30.7 (7)	2.38 (22)					100.74
	pl (7)	54.0 (5)		28.8 (3)		0.53 (5)		0.28 (3)	12.0 (3)	4.08 (13)	0.32 (3)			100.01
85-41c	**200 MPa**													
85-41c#5														
	gl (17)	60.4 (5)	0.66 (3)	17.3 (2)		4.62 (9)	0.11 (2)	4.44 (5)	7.36 (16)	3.81 (18)	0.95 (4)	0.24 (2)	0.03 (2)	94.41[d]
	ol (9)	39.7 (3)		0.03 (1)	0.01 (2)	13.3 (3)	0.21 (2)	46.5 (4)	0.21 (1)				0.08 (3)	100.04
	cpx (7)	53.6 (3)	0.27 (7)	1.79 (27)	0.70 (15)	4.72 (59)	0.14 (1)	18.4 (5)	20.9 (6)	0.14 (5)				100.66
85-41c#7														
	gl (15)	61.7 (5)	0.70 (3)	18.4 (3)		4.18 (14)	0.09 (2)	3.07 (19)	6.33 (27)	4.13 (17)	1.09 (4)	0.23 (3)	0.04 (2)	93.45
	ol (9)	39.1 (3)	0.02 (1)	0.03 (3)	0.04 (5)	17.2 (2)	0.24 (3)	43.1 (2)	0.18 (3)				0.11 (4)	100.02
	cpx (5)	52.7 (4)	0.42 (2)	2.36 (21)	0.49 (8)	5.69 (12)	0.17 (2)	17.1 (3)	21.5 (2)	0.17 (9)				100.60
	opx (6)	55.5 (3)	0.19 (2)	1.64 (18)	0.25 (7)	11.5 (4)	0.23 (2)	30.0 (4)	1.37 (8)					100.68
	sp (4)	0.31 (33)	0.74 (15)	13.0 (20)	46.4 (3.4)	29.4 (1.8)	0.28 (4)	8.41 (34)	0.26 (3)				0.05 (2)	98.85

85-41c#8														
	gl (21)	62.7 (5)	0.89 (3)	17.7 (2)		4.21 (12)	0.08 (2)	2.59 (11)	5.39 (15)	4.60 (17)	1.46 (4)	0.33 (5)	0.04 (2)	96.86
	cpx (4)	52.8 (5)	0.50 (5)	2.23 (31)	0.44 (19)	6.28 (38)	0.16 (4)	17.9 (7)	19.8 (6)	0.17 (4)				100.28
	pl (5)	53.8 (6)		28.8 (4)		0.78 (12)		0.26 (11)	11.7 (6)	4.26 (33)	0.20 (7)			99.80
	opx (5)	55.4 (6)	0.25 (6)	1.28 (36)	0.13 (3)	13.0 (3)	0.23 (2)	28.0 (4)	2.04 (20)	0.03 (2)				100.36
85-41c#9														
	gl (8)	65.6 (2)	0.47 (4)	17.6 (2)		3.55 (6)	0.04 (2)	1.75 (11)	4.63 (13)	4.70 (19)	1.50 (2)	0.23 (3)		93.8
	cpx (6)	52.3 (3)	0.58 (7)	2.39 (35)	0.18 (4)	7.22 (45)	0.16 (5)	16.1 (2)	20.3 (3)	0.28 (3)				99.5
	opx (6)	54.6 (4)	0.24 (2)	1.49 (21)	0.07 (1)	15.0 (4)	0.28 (5)	27.2 (3)	1.33 (9)	0.08 (5)				100.2
	pl (4)	53.5 (3)		29.4 (5)		0.64 (9)		0.21 (4)	12.1 (4)	4.35 (23)	0.13 (4)			100.4
85-44	**200 MPa**													
85-44#3														
	gl (9)	56.7 (4)	0.86 (5)	18.8 (3)	0.04 (2)	6.35 (14)	0.16 (7)	4.05 (13)	8.19 (24)	4.07 (15)	0.59 (4)	0.21 (3)		93.42
	ol (5)	38.6 (7)	0.01 (1)	0.07 (3)	0.04 (3)	19.1 (7)	0.30 (3)	40.9 (7)	0.27 (2)				0.16 (3)	99.45
	pl (7)	48.4 (5)		32.1 (5)		0.74 (12)		0.38 (14)	16.7 (3)	2.06 (10)	0.05 (1)			100.43
	cpx (10)	52.5 (5)	0.59 (9)	3.14 (51)	0.63 (11)	6.23 (38)	0.15 (3)	16.4 (4)	20.9 (6)	0.28 (3)				100.82
	sp (5)		1.55 (1.53)	16.7 (3.7)	38.1 (4.2)	32.9 (6.9)	0.41 (4)	9.10 (1.92)	0.23 (10)				0.24 (3)	99.23
85-44#4														
	gl (8)	58.0 (4)	0.92 (4)	18.6 (2)	0.03 (4)	6.01 (10)	0.20 (5)	3.51 (7)	7.31 (18)	4.62 (7)	0.64 (3)	0.21 (3)		93.19
	ol (5)	38.3 (3)	0.03 (2)	0.10 (3)	0.04 (1)	21.8 (3)	0.31 (4)	38.8 (6)	0.27 (2)				0.14 (2)	99.79
	pl (11)	48.3 (6)		32.3 (8)		0.64 (21)		0.19 (17)	16.1 (6)	2.30 (15)	0.05 (2)			99.88
	cpx (11)	51.8 (6)	0.63 (10)	3.02 (44)	0.54 (8)	6.86 (88)	0.18 (4)	16.0 (6)	20.9 (9)	0.28 (4)				100.21
	sp (5)		0.80 (28)	19.1 (3.4)	37.4 (1.8)	32.4 (3.8)	0.40 (2)	9.09 (1.28)	0.27 (9)				0.23 (4)	99.69
85-44#5														
	gl (7)	59.5 (3)	0.96 (2)	18.3 (2)	0.07 (4)	5.68 (12)	0.14 (2)	2.86 (4)	6.27 (26)	5.20 (18)	0.75 (3)	0.23 (2)		93.54
	amp (6)	42.8 (5)	3.07 (12)	12.4 (3)	0.92 (20)	8.85 (9)	0.13 (2)	15.0 (3)	11.5 (1)	2.75 (8)	0.22 (2)			97.64
	ol (6)	38.2 (6)	0.02 (2)	0.11 (3)	0.03 (2)	22.5 (5)	0.34 (2)	38.8 (8)	0.25 (2)				0.14 (2)	100.39
	pl (8)	49.1 (7)		32.4 (1.0)		0.65 (13)		0.17 (11)	16.0 (6)	2.39 (12)	0.06 (3)			100.77
	cpx (8)	52.1 (6)	0.67 (11)	3.06 (32)	0.46 (10)	6.99 (49)	0.19 (3)	15.8 (4)	20.9 (7)	0.29 (4)				100.46
	sp (7)	0.09 (24)	1.23 (1.75)	18.8 (4.8)	37.5 (2.6)	32.6 (6.1)	0.42 (5)	8.60 (1.80)	0.25 (8)				0.23 (3)	99.72
85-44#6														
	gl (8)	57.0 (4)	0.80 (3)	19.0 (2)	0.02 (2)	5.98 (11)	0.11 (4)	4.16 (10)	8.19 (14)	4.17 (19)	0.58 (2)		0.01 (1)	94.63
	ol (8)	38.9 (2)	0.10 (3)	0.05 (6)	0.03 (3)	18.6 (7)	0.26 (2)	41.9 (8)	0.28 (3)					100.12
85-44#7														
	gl (8)	54.2 (2)	0.70 (3)	19.0 (1)	0.01 (1)	6.31 (14)	0.15 (3)	5.64 (9)	10.3 (1)	3.24 (16)	0.43 (3)		0.01 (1)	94.84
	cpx (13)	51.7 (4)	0.40 (7)	3.59 (33)	0.77 (13)	4.60 (33)	0.11 (4)	16.5 (5)	21.9 (7)	0.24 (13)				99.81
	ol (9)	39.3 (2)	0.07 (3)	0.10 (4)	0.10 (3)	14.8 (1)	0.18 (4)	45.5 (4)	0.30 (5)					100.35
	sp (1)	0.09	1.33	17.9	37.9	30.1	0.31	10.7	0.25	0.25				99.92
85-44	**800 MPa**													
B372														
	ol (5)	40.4 (4)	0.02 (1)	0.03 (1)	0.03 (2)	12.5 (4)	0.14 (1)	47.0 (7)	0.14 (3)				0.04 (2)	100.3
B373														
	gl (6)	57.2 (2)	0.57 (2)	17.1 (2)	0.01 (1)	6.80 (11)	0.14 (2)	4.98 (15)	8.85 (13)	1.21 (12)	0.29 (2)			85.76
	amp (10)	45.2 (4)	0.71 (5)	12.4 (2)	0.25 (11)	7.90 (18)	0.09 (1)	17.0 (2)	11.1 (1)	2.07 (12)	0.21 (2)			96.8
	cpx (9)	53.1 (5)	0.24 (8)	2.38 (48)	0.25 (25)	6.56 (48)	0.17 (2)	16.9 (6)	20.2 (1.0)	0.22 (3)				100.0
	opx (7)	55.5 (6)	0.06 (1)	1.61 (10)	0.20 (4)	12.8 (2)	0.28 (2)	28.2 (4)	1.29 (4)					99.9

Table 3 (Contd.)

Run no.	Phase[a]	SiO_2	TiO_2	Al_2O_3	Cr_2O_3	FeO	MnO	MgO	CaO	Na_2O	K_2O	P_2O_5	NiO	Total
B380	gl (4)	59.1 (2)	0.39 (2)	19.7 (1)	0.04 (3)	5.86 (4)	0.14 (2)	3.69 (6)	8.22 (8)	2.24 (18)	0.72 (2)			85.66
	amp (4)	44.4 (4)	0.70 (4)	12.9 (4)	0.12 (10)	8.20 (82)	0.10 (2)	16.5 (4)	11.3 (4)	2.34 (3)	0.25 (1)			96.8
	cpx (5)	52.1 (6)	0.25 (9)	2.58 (55)	0.11 (11)	6.71 (63)	0.21 (3)	16.8 (6)	20.9 (9)	0.25 (2)				99.6
	sp (4)	0.11 (3)	0.28 (4)	24.1 (2.2)	39.2 (1.5)	23.9 (4.6)	0.30 (9)	11.5 (2.3)	0.29 (5)					99.8
A1.2	gl (13)	57.8 (3)	0.73 (1)	17.6 (1)	0.00 (1)	4.07 (16)	0.04 (1)	6.16 (6)	9.03 (11)	3.19 (14)	0.58 (2)	0.12 (2)	0.00 (1)	99.32
	opx (15)	54.3 (4)	0.14 (2)	4.69 (53)	0.24 (2)	6.70 (14)	0.09 (1)	30.9 (4)	2.16 (8)	0.1 (1)				99.32
	cpx (23)	52.2 (5)	0.24 (2)	5.84 (38)	0.32 (2)	4.59 (14)	0.10 (2)	19.6 (3)	15.8 (6)	0.62 (4)				98.69

[a] *gl* Glass; *ol* olivine; *cpx* clinopyroxene; *pl* plagioclase; *sp* spinel; *amp* amphibole

[b] Number of microprobe analyses

[c] One standard deviation of replicate analyses in terms of least unit cited. Thus 56.5 (3) should be read as 56.5 ± 0.3

[d] Analyses of hydrous glasses are normalized to 100% with all Fe reported as FeO. Unnormalized total is reported

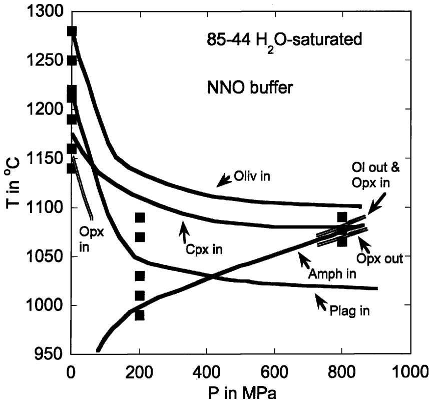

Fig. 2 Pressure–temperature diagram showing the results of phase equilibrium experiments performed on 85-44 under H_2O-saturated conditions at the NNO buffer at 200 and 800 MPa (see Tables 2 and 3 for durations and compositions). The 0.1-MPa experiments were carried out at the QFM buffer and results from 85-44 (near liquidus) and a compositionally similar primitive basaltic andesite (82-94a) are reported in Baker at al. (1994). *Black squares* indicate an experimental data point. *Lines* indicate the effect of pressure and H_2O content on phase appearance temperature. The oliv in curve is inferred from results of Sisson and Grove (1993a). The plag in boundary at 800 MPa is inferred from the experiments of Holloway and Burnham (1972). The phase appearance boundaries reported here are very similar to those obtained by Holloway and Burnham (1972) on the 1921 Kilauea basalt using 58% CO_2–42%H_2O and NNO (see their Fig. 3)

experimental results on 85-44 (Baker et al. 1994) place the liquidus above 1,280 °C. The Baker et al. experiments were performed under anhydrous conditions at the QFM buffer. Lower temperature phase appearances were taken from experiments on 82–94a (Baker et al. 1994), which is similar in composition to 85-44. Also shown are the 200- and 800-MPa H_2O-saturated experiments carried out at the Ni–NiO buffer. At the highest temperature investigated at 200 MPa (1,090 °C, Table 2), the experimental charge is ~96% melt with a small amount of olivine (oliv) and high-Ca pyroxene (cpx). Based on direct measurements of the effect of H_2O on the melting relations of basalts (Sisson and Grove 1993a), the liquidus is inferred to be at ~1,150 °C. At 1,070 °C, oliv, cpx, and an iron-rich Al-Cr spinel (sp) coexist. At 1,030 °C, plagioclase (plag) has joined the crystallization sequence, and the liquid has evolved to a high-Al andesite with 18.8% Al_2O_3 at ~57 wt% SiO_2. Amphibole (Mg# = Mg/[Mg + Fe^{2+}] molar = 0.75), oliv, cpx, sp, and plag coexist at the lowest temperature investigated (990 °C). Under these conditions the charge is > 55% crystalline and the liquid is andesitic (59.7% SiO_2 and 18.3% Al_2O_3). Based on phase relations at 0.1 and 800 MPa, orthopyroxene (opx) is inferred to appear at a lower temperature, where it would be in reaction relation with oliv and liquid.

At 800 MPa, the high temperature experiment (1,090 °C) contained > 95% quenched melt and oliv. The liquidus temperature was not determined. Both cpx and oliv are present in the 1,077 °C experiment. At 1,065 °C, oliv is no longer a part of the mineral assemblage, and opx and a magnesian (Mg# = 0.80) pargasite amphibole (amph) join cpx. The higher Mg# of amph is a result of its appearance closer to the liquidus. At the lowest temperature investigated (1,045 °C) opx reacts with amph, leading to the disappearance of opx and a liquid that coexists with amph, cpx, and sp. At these low temperatures and high H_2O contents the 800 MPa derivative liquids are high alumina andesites (59% SiO_2 and 20% Al_2O_3). Müntener et al. (2001) observed similar enrichments in Si and Al in their 800-MPa experiments on 85-44. At a lower temperature, plagioclase is inferred to join the crystallizing assemblage.

The pressure–temperature relations found for 85-44 are similar to those found by Holloway and Burnham (1972) for the 1921 Kilauea basalt. The Holloway and Burnham (1972) study used a mixed CO_2–H_2O (42% CO_2 and 58% H_2O, molar) fluid, and their experiments were also buffered at Ni–NiO. In both sets of experiments the appearance temperature of amph increases with increasing pressure by approximately 100 °C from 200 to 800 MPa, and amph becomes more magnesian because it appears closer to the liquidus. Plagioclase appearance temperature decreases by > 150 °C over the 0.1–800-MPa pressure interval.

Primitive magnesian andesite 85-41c

In comparison to the basaltic andesite, this composition contains much higher SiO_2 (57.9 wt%) and lower Al_2O_3 (14.6 wt%). At 0.1 MPa, under anhydrous conditions, oliv is the liquidus phase at ~1,250 °C and sp joins oliv by 1,225 °C. Orthopyroxene and plag have joined the crystallization assemblage by 1,200 °C, and oliv + liquid react to form opx over the temperature range of 1,200 to 1,167 °C. After oliv has been removed by reaction, opx, cpx, and plag co-crystallize to the lowest temperature investigated.

At 200 MPa, the primitive magnesian andesite has oliv and cpx as liquidus phases at the highest temperature investigated (1,040 °C). Figure 3 shows the 200-MPa phase appearance sequence for both 85-41c and 85-44. In 85-41c, opx and sp appear as crystallizing phases at ~1,030 °C, and oliv reacts with melt and disappears from the crystallizing assemblage at ~1,000 °C. In the lower temperature experiments (980 and 940 °C) plag crystallizes along with opx, cpx, and sp.

The difference in the phase appearance sequences at 200 MPa, H_2O-saturated in 85-44 and 85-41c, are a result of the higher SiO_2 and lower Al_2O_3 contents of 85-41c. This leads to the appearance of opx in 85-41c before plag (Fig. 3). In contrast, opx has not appeared at the lowest temperature investigated in 85-44 and plag saturation occurs at a higher temperature ~50 °C higher in 85-44.

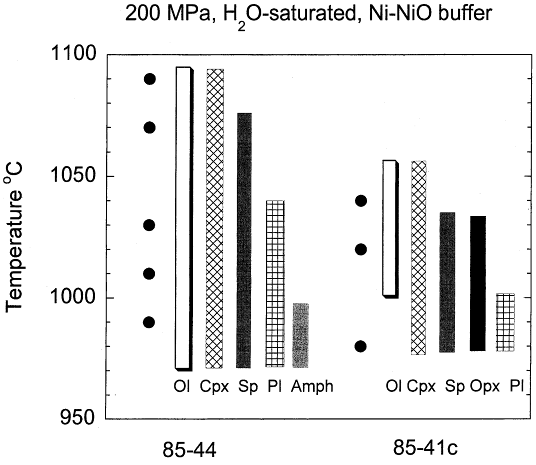

Fig. 3 Phase appearance sequences for the primitive basaltic andesite (85-44) and primitive magnesian andesite (85-41c) at 200 MPa, H_2O-saturated at the NNO buffer. See Tables 2 and 3 for experimental conditions and phase compositions. In 85-44, plag appears after oliv + cpx + sp, and amphibole (amph) has just appeared in the lowest temperature experiment. In contrast, the phase appearance sequence in the high-SiO_2, low-Al_2O_3 primitive magnesian andesite is oliv, followed by cpx and sp. Opx is the next phase to appear in reaction relation with oliv. Plag is the last phase to appear in the lowest temperature experiment. The lowest temperature experiment at 940 °C contains the same assemblage present at 980 °C

Composition A and 85-44

Experiments on the modified primitive andesite composition (A) with 4.5 wt% H_2O added at 1 to 1.3 GPa (Table 2) are shown in Fig. 4 along with the results of Baker et al. (1994) for 85-44 at 1 GPa and variable H_2O content. Both compositions have pyroxene as the liquidus phase under anhydrous conditions at 1.0 to 1.5 GPa. Under H_2O-undersaturated conditions, the addition of 4.5 to 6 wt% H_2O is sufficient to bring oliv and opx simultaneously to the liquidus at 1 GPa. For composition A, the liquid is saturated with oliv, opx, and cpx at ~1,175 °C and 1 GPa. For 85-44, the 1-GPa experiments performed by Baker et al. (1994) indicate that ~4.5 wt% H_2O would be necessary to saturate with oliv and opx on the liquidus.

These H_2O-undersaturated results indicate that the primitive basaltic andesite and magnesian andesite must contain at least 4.5 wt% H_2O to be in equilibrium with a mantle harzburgite (oliv + opx) residual assemblage at a depth of 30 km beneath Mt. Shasta. This is the measured depth to the Moho beneath Mt. Shasta (Fuis et al. 1987), and represents a minimum estimate of pre-eruptive H_2O content necessary to saturate these primitive melts with a mantle residue assemblage. These minimum pre-eruptive H_2O contents coincide with pre-eruptive H_2O estimates based on mineral compositional evidence (Baker et al. 1994) and measured H_2O contents in melt inclusions (Anderson 1979; Sisson and Layne 1993). It is possible for these two compositions to be in equilibrium with ol + opx over a range of pressure, temperature, and H_2O contents. Olivine and opx could be sustained as liquidus phases as pressure increases by an increasing melt H_2O content and decreasing temperature. This effect can be inferred by comparing the H_2O-saturated liquidus phase relation for 85-44 (Fig. 2) with the

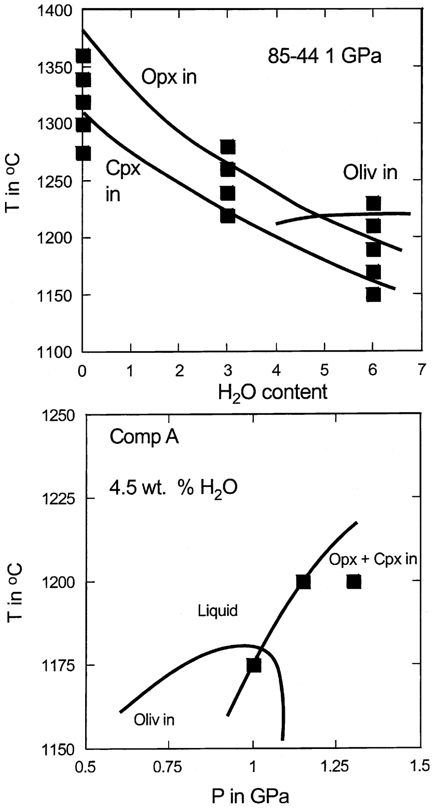

Fig. 4 Results of high-pressure experiments on the Mt. Shasta region primitive lavas at H_2O-undersaturated conditions. *Upper diagram* shows the effect of variable H_2O at 1 GPa on the liquidus phase relations of 85-44 (Baker et al. 1994). Approximately 4.5 wt% H_2O is required to saturate 85-44 with a harzburgitic mantle residual assemblage. *Lower diagram* shows the results of variable pressure on the liquidus phase appearance sequence of 85-41c. At 1 GPa, oliv + opx + cpx are near liquidus phases with 4.5 wt% H_2O

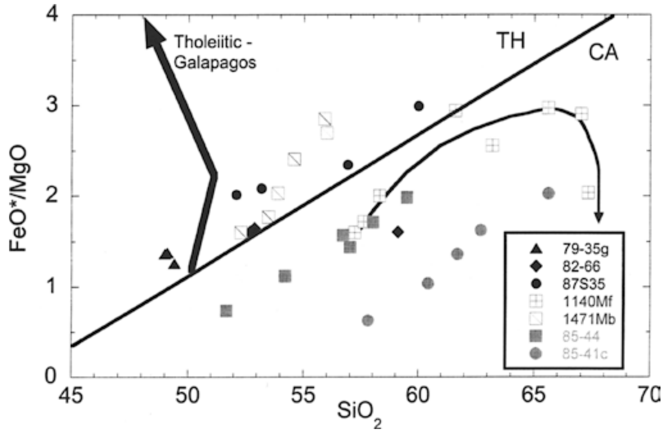

Fig. 5 Experimental liquids projected on the FeO*/MgO vs. SiO_2 diagram. All compositions are renormalized to an anhydrous basis. The tholeiitic (TH)–calc-alkaline (CA) dividing line is from Miyashiro (1974). The *black symbols* (79–35 g, 82-66 and 87S35) are liquid lines of descent followed by low-SiO_2 high-Al_2O_3 basalts at 200 MPa and NNO (Sisson and Grove 1993a). These liquid lines of descent define trends similar to the differentiation trends found in many subduction related magmatic suites. Near *vertical arrow* shows tholeiitic differentiation trend exhibited by Galapagos MORB lavas (Grove and Baker 1984; Juster et al. 1989). Also shown are liquid lines of descent followed by the 200 MPa experiments on the primitive high-SiO_2, low Al_2O_3 lavas from the Mt. Shasta region (85-44 and 85-41c, *gray symbols*). These liquid lines of descent follow calc-alkaline trends defined by many subduction-related high-magnesian andesite suites. The results of experiments on high-alumina basalt, 1471Mb (Wagner et al. 1995), at 100 MPa and NNO also show more FeO enrichment as a result of lower H_2O contents. The 100-MPa experiments on andesite 1140Mf (Grove et al. 1997) are included to show the differentiation path for SiO_2-rich residual liquids at low temperatures and high-SiO_2 contents. An increase in the proportion usp/Fe–Mg silicate results in rapid FeO depletion at the NNO buffer (*arrow* illustrates trend)

H_2O-undersaturated boundaries (Fig. 4). Under H_2O-saturated conditions ol + opx should be liquidus phases at 1 GPa and ~1,100 °C (Fig. 2). Melt H_2O contents under H_2O-saturated conditions would be ~16 wt% (Hamilton et al. 1964 and 85-44 would be 800 MPa for glass analyses, Table 3). If the ol + opx saturation boundary in Fig. 4 is extended to higher melt H_2O contents, a similar value of liquid H_2O content would be inferred.

Discussion

Role of fractional crystallization in producing calc-alkaline differentiation trends

Compositional variations in FeO/MgO vs. SiO_2*

Miyashiro (1974) introduced the FeO*/MgO vs. SiO_2 diagram and used it to discriminate calc-alkaline from tholeiitic differentiation trends and to distinguish among different types of calc-alkaline trends that were found in various arc environments. On the Miyashiro (1974) diagram, an anhydrous fractional crystallization trend (tholeiitic trend) is nearly vertical, with FeO*/MgO increasing continuously at constant SiO_2. The tholeiitic trend (Fig. 5) is followed during fractional crystallization of basalt at low pressure, anhydrous conditions, and an excellent example is the differentiation trend of Galapagos mid-ocean ridge lavas (Grove and Kinzler 1986; Juster et al. 1989). The strong near vertical increase of FeO*/MgO at constant SiO_2 results from the early appearance of plag as a crystallizing phase, a high proportion of plag/Fe–Mg silicates in the crystallizing assemblage, the late appearance of sp as a crystallizing phase, and the high SiO_2 content of the Na-rich crystallizing plag. Sisson and Grove (1993a) demonstrated that liquids produced by crystallization of hydrous basaltic magmas at modestly oxidizing conditions (Ni–NiO buffer) define crystallization paths similar to those found in many calc-alkaline suites. The presence of ~6 wt% H_2O in the 200-MPa liquids has a significant effect on the phase appearance sequence and, therefore, on the liquid line of descent followed during crystallization. The influence of H_2O is to expand the primary phase volumes for oliv and cpx and shrink the plag primary phase volume, causing ferromagnesian minerals to crystallize early and plag to crystallize late. In addition,

H_2O lowers the temperature at which silicate minerals crystallize, but has little effect on the appearance temperature of sp. Thus, an iron-rich Cr–Al sp appears at or near the liquidus of a hydrous basalt melt (Sisson and Grove 1993a). When plag appears as a crystallizing phase, it is Ca- and Al-rich and SiO_2 poor, which promotes enrichment of SiO_2 and alkalis in the residual liquids. Therefore, liquids produced by fractional crystallization become depleted in FeO and enriched in SiO_2; the calc-alkaline differentiation trend.

The liquids from the 200-MPa H_2O-saturated crystallization experiments for the primitive basaltic andesite (85-44) and andesite (85-41c) are plotted in Fig. 5 along with the 200-MPa data of Sisson and Grove (1993a) on basaltic compositions. The crystallization paths followed by these primitive basaltic andesite and andesite compositions parallel those of the Sisson and Grove (1993a) experiments, and also follow a calc-alkaline differentiation trend. These differentiation trends begin at a lower value of FeO*/MgO, and extend along a path that parallels the Sisson and Grove 200 MPa H_2O-saturated experimental trend. The 85-44 and 85-41c crystallization paths plot in this portion of the FeO*/MgO vs. SiO_2 diagram because the parent magmas contain lower FeO*/MgO and higher SiO_2 than the parental melts that were examined by Sisson and Grove (1993a). Otherwise, the slopes of the trends are fairly similar, reflecting similar proportions of minerals in the crystallizing assemblage and similar influences of mineral composition on the crystallization paths.

Also shown in Fig. 5 are 100- and 200-MPa H_2O-saturated experiments on basalts and basaltic andesites from Medicine Lake volcano (Wagner et al. 1995, 1471Mb; Grove et al. 1997, 1140Mf). The 1471Mb experiments have a slightly steeper slope than the calc-alkaline trends of Sisson and Grove (1993a), reflecting the lower pressure (100 MPa) of the 1471Mb experiments. The effect of lower H_2O-saturated pressure is to cause plag to appear earlier in the crystallization sequence and to increase the proportion of plag relative to Fe–Mg silicates in the crystallizing assemblage. Both effects lead to a steeper slope for the 1471Mb trend. In 1471Mb, the proportions of plag/Fe–Mg silicates is ~1.5 whereas the proportion of plag/Fe–Mg silicates in the 200 MPa H_2O-saturated experiments on 79-35g is 0.6. The shallower slopes of the 200 MPa H_2O-saturated differentiation trends on the FeO*/MgO vs. SiO_2 diagram are caused by three factors: the decrease in plag/Fe–Mg silicate proportions, the earlier appearance of sp and the effect of higher melt H_2O that lowers the SiO_2 in the crystallizing plag.

Sample 1140Mf is petrologically and geochemically similar to Mt. Shasta primitive basaltic andesites (Kinzler et al. 2000) and can be produced from a magma similar to 85-44 by fractional crystallization of oliv + cpx + plag at 100 to 200 MPa. Since 1140Mf has 56.3 wt% SiO_2 (Table 1), experiments could be extended to lower temperatures allowing the higher SiO_2 portion of the liquid line of descent to be examined. The trend is illustrated in Fig. 5 with the curved arrow for the 100-MPa experiments. The vertical descent of residual liquids to low FeO*/MgO coincides with the disappearance of oliv from the crystallization assemblage, and the appearance of opx, along with cpx, plag, and magnetite–ulvöspinel (usp). The abrupt decrease in FeO*/MgO is a consequence of the increase in the proportion of spinel in the opx + cpx + plag + usp assemblage, relative to the higher temperature oliv + cpx + plag + usp assemblage.

Compositional variations in mineral component space

The bulk compositions of 85-44 and 85-41c and the liquids produced in the 200-MPa H_2O-saturated experiments are projected into the Oliv (forsterite + fayalite)-Plag (anorthite + albite)-Qtz (SiO_2) and Oliv-Cpx (diopside + hedenbergite)-Qtz pseudoternaries in Fig. 6 using the projection scheme of Tormey et al.

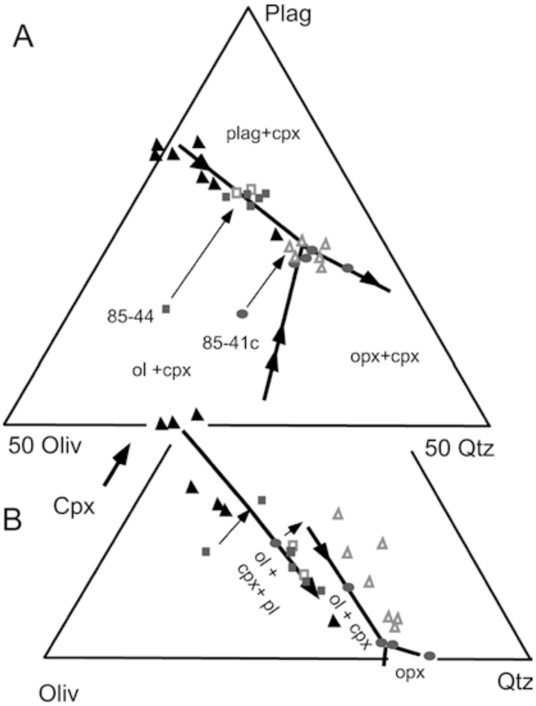

Fig. 6 Compositions of 200-MPa, NNO, H_2O-saturated liquids on the pseudoternary projections: **A** Olivine (*Oliv*)-Plagioclase (*Plag*)-Quartz (*Qtz*) projected from Clinopyroxene (*Cpx*) showing only the upper half of the triangle from 50% Oliv-50% Qtz to 100% Plag. **B** Oliv-Cpx-Qtz projection scheme from plag. Projection scheme is from Tormey et al. (1987) and Grove (1993). The *upper half of the triangle* is not shown. Experimental liquids from Sisson and Grove (1993a) are shown as *black triangles*. The three triangles that plot near the 50 oliv–50 qtz base belong to projection **B**. Experimental liquids from 85-44 are shown as *gray squares* and 85-41c experiments are plotted as *gray ovals*. Also shown are experiments of Moore and Carmichael (1998; *open squares*) and Blatter and Carmichael (1998; *open triangles*). *Dark lines* are saturation and reaction boundaries. *Arrows* show direction of liquid evolution with decreasing temperature. *Double arrows* indicate a reaction boundary (oliv + opx + cpx in **A**). The *dark lines* in **A** join at the oliv + opx + cpx + plag + sp reaction. *Lighter arrows* in **A** and **B** indicate crystallization paths followed by the 85-44 and 85-41c from liquidus conditions

Table 4 Mass balance models of mantle melting reactions

1. MBC[a]												
	SiO_2	TiO_2	Al_2O_3	FeO	MnO	MgO	CaO	Na_2O	K_2O	Sum	Mg#	FeO/MgO
Mantle Melt[a]	47.8	0.66	19.2	7.61	0.0	11.0	11.2	2.42	0.11	100	0.72	0.692
G&G98[b]												
	MM[a]	±	Cpx	±	Opx	±	Oliv			ΣR^2	Opx[c]	Oliv[c]
B392	0.96	–	0.08	+	0.29	–	0.19			1.1	+1	−0.65
B384	0.86	+	0.0	+	0.23	–	0.11			3.1	+1	−0.48
B388	0.84	+	0.0	+	0.27	–	0.12			2.2	+1	−0.44
2. PRM[d]												
%melt	SiO_2	TiO_2	Al_2O_3	FeO	MnO	MgO	CaO	Na_2O	K_2O	Sum	Mg#	FeO/MgO
0.18	51.5	0.62	16.6	6.83	0.0	12.2	10.1	2.05	0.09	100.	0.76	0.557
0.21	53.7	0.61	15.1	6.33	0.0	12.8	9.48	1.83	0.08	100.	0.78	0.494
0.26	55.6	0.59	13.9	5.90	0.0	13.4	8.96	1.61	0.08	100.	0.80	0.441
3. NLM[e]												
Shasta												
85-41c	MM[a]	±	Cpx	±	Opx	±	Oliv	±	Fluid	ΣR^2	Opx[c]	Oliv[c]
	0.51	+	0.0	+	1.1	–	0.61	+	0.02	7.1	+1	−0.55
85-44	MM[a]											
	0.74	+	0.05	+	0.41	–	0.22	+	0.01	3.9	+1	−0.54

[a] 1. *MBC* mass balance calculation. Mantle melt (MM) is the average of three liquids (B304, B330, and B329) reported in Gaetani and Grove (1998) that are saturated with the mantle residue assemblage (oliv + opx + cpx + spinel at 1.2 GPa under H_2O-undersaturated conditions ~6 wt% H_2O)

[b] Compositions B392, B384, and B388 are liquids from basalt + peridotite mixtures reported in Gaetani and Grove (1998). B392 is saturated with oliv + opx + cpx. B384 and B388 are saturated with oliv + opx. Results of mass balance calculations are shown for creating these three liquids from the lower temperature 4-phase saturated mantle melt (MM). Negative coefficients indicate that the phase crystallizes, positive coefficients indicate dissolution

[c] Stoichiometric coefficients of the reaction normalized to one unit of liquid in weight units

[d] 2. *PRM* Peridotite reaction melting model calculates liquid compositions of harzburgite melt. Melt compositions are calculated from the average mantle melt (MM) by removing olivine and adding orthopyroxene in weight proportions 1.0:0.48. Modeling was carried out in 2 wt% increments adding phases that were calculated to be in Fe–Mg exchange with the liquid at each step assuming an oliv–melt $K_D^{Fe\text{-}Mg}(K_D^{Fe\text{-}Mg}=[X_{Fe}^{Ol}X_{Mg}^{Liq}]/[X_{Mg}^{Ol}X_{Fe}^{Liq}])=0.29$ and an opx–melt $K_D^{Fe\text{-}Mg}=0.27$. Numbers below % melt indicate weight fraction of total solid reacted per initial mass of liquid. Final value represents the extreme of the mantle melting/reaction trends plotted in Figs. 7 and 8

[e] 3. *NLM* Natural lava melting model is a calculation using experimental liquids and Shasta region lavas. Model mass balance calculation uses MM, cpx, opx, oliv, and the major elements (Na_2O and K_2O) from the subduction zone fluid-rich component (fluid) from Table 5of Grove et al. (2002) to make primitive Shasta lavas 85-41c and 85-44

(1987). Also shown are multiply saturated liquids of high-alumina basalts from Medicine Lake volcano (Sisson and Grove 1993a) and experiments that established high H_2O contents in Mexican Volcanic Belt lavas (Blatter and Carmichael 1998; Moore and Carmichael 1998). Figure 6a shows the projection through Cpx and is especially useful because most of the 200 MPa liquids are saturated with clinopyroxene. The projection from Plag shown in Fig. 6b is also useful, as it illustrates the silica enrichment exhibited by these lavas during crustal level crystallization under H_2O-saturated conditions.

The 200-MPa experimentally produced liquids for the 85-44 composition that coexist with oliv + plag + cpx + sp define a multiple saturation boundary in Fig. 6a, b that coincides with the oliv + plag + cpx boundary defined by Sisson and Grove (1993a). The principal difference in primitive basaltic andesite 85-44 is that it has an appreciable interval of oliv +cpx crystallization, before it becomes saturated with plag. The oliv + plag + cpx-saturated liquids obtained by Moore and Carmichael (1998) on a magnesian basaltic andesite from the Mexican volcanic belt (Mas-25, Table 1) are coincident with the 85-44 liquids. For 85-41c, oliv + cpx ±sp are the liquidus phases at 200-MPa H_2O-saturated conditions, followed by the appearance of opx, and then followed by plag saturation (Fig. 6a). In the Oliv-Cpx-Qtz pseudoternary (Fig. 6b), the oliv + cpx liquids from 85-41c plot at higher qtz values than those from 85-44, and do not coincide with the oliv + plag + cpx saturation boundary. Olivine reacts with liquid to form opx over a 40 °C temperature interval in 85-41c, oliv is exhausted from the phase assemblage, and the liquid leaves the reaction boundary and follows the opx + cpx + plag-saturation boundary. Experimental studies have also been carried out by Blatter and Carmichael (1998) on a high H_2O, primitive magnesian andesite from the western Mexican Volcanic Belt (MAS-911, Table 1). This composition shows a similar crystallization sequence (Fig. 6) to the one observed for 85-41c. Note that the oliv + cpx saturated liquids in MAS-911 plot at higher SiO_2 values than the 85-41c liquids saturated with a similar phase assemblage. This is most likely a consequence of the higher alkali content of MAS-911 (in MAS-911 $Na_2O + K_2O = 5.5$ wt% vs. 3.8 wt% in 85-41c), which has the effect of expanding the olivine primary phase volume (Grove and Juster 1989; Longhi 1991).

Role of hydrous mantle melting in producing calc-alkaline differentiation trends

Both Shasta region lavas are very primitive despite their high SiO_2 contents. Composition A is multiply saturated

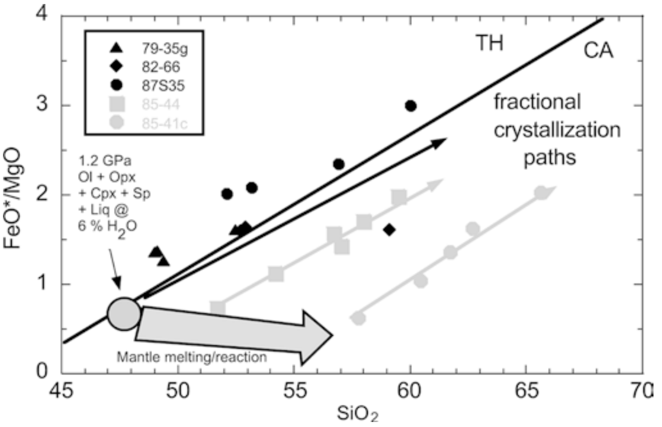

Fig. 7 Experimental liquids projected on the FeO*/MgO vs. SiO_2 diagram. The tholeiitic (TH)–calc-alkaline (CA) dividing line is from Miyashiro (1974). *Symbols* are the same as those used in Fig. 5. *Lines with arrows* illustrate the liquid lines of descent followed by primitive melts as they experience crystal fractionation under hydrous conditions at 200 MPa and the NNO buffer. The *large circle* plotting on the TH-CA dividing line marks the locus of primitive mantle hydrous melts derived at 1.2 GPa (Gaetani and Grove 1998) and coexisting with oliv + opx + cpx + sp. These liquids follow a differentiation trend similar to that defined by the Sisson and Grove (1993a) liquids (*black arrow*) at 200 MPa H_2O-saturated. The *gray arrow* that trends to high-SiO_2 and low FeO*/MgO is the path followed during mantle melting at 1.2-GPa and 6 wt% H_2O (Table 4) after cpx and sp are exhausted from the mantle residue. This melting path lies on the oliv + opx reaction boundary

on its liquidus with oliv + opx at 1 GPa with 4.5 wt% H_2O added. The inferred pre-eruptive H_2O content for 85-41c (Anderson 1979) is 6.5 wt% H_2O, so the multiple saturation depth and temperature may be higher than that given by the 4.5 wt% H_2O experiments. Baker et al. (1994) showed that 85-44 is saturated with oliv + opx on its liquidus at ~4.5 wt% H_2O and 1 GPa. This magmatic H_2O content also corresponds with the pre-eruptive H_2O content estimated for 85-44 (Anderson 1979; Baker et al. 1994). The pressure of 1.0 GPa is equivalent to the depth to the top of the mantle wedge beneath Mt Shasta. Both of the magmas are in equilibrium with a mantle residue assemblage representative of high extents of melting under hydrous (H_2O-undersaturated) conditions (Fig. 4). The basaltic andesite (85-44) contains oliv phenocrysts of $Fo_{89.6}$. Sample 85-41c contains $Fo_{93.6}$ olivine. Thus, 85-41c represents a higher extent of mantle melting than 85-44.

Melting experiments on mantle peridotite under H_2O-undersaturated conditions have been carried out by Kushiro (1990), Hirose and Kawamoto (1995), Hirose (1997), and Gaetani and Grove (1998). Gaetani and Grove (1998) provide the most complete characterization of the mantle-melting reaction when the residue contains oliv + opx + cpx + sp from 1.2 to 1.6-GPa. They present experimental data on 60% peridotite: 40% 85-44 mixture that can be used to calculate the mantle melting reaction extended beyond the point of exhaustion of sp and cpx. The results of the Gaetani and Grove (1998) experiments at 1.2-GPa have been used to

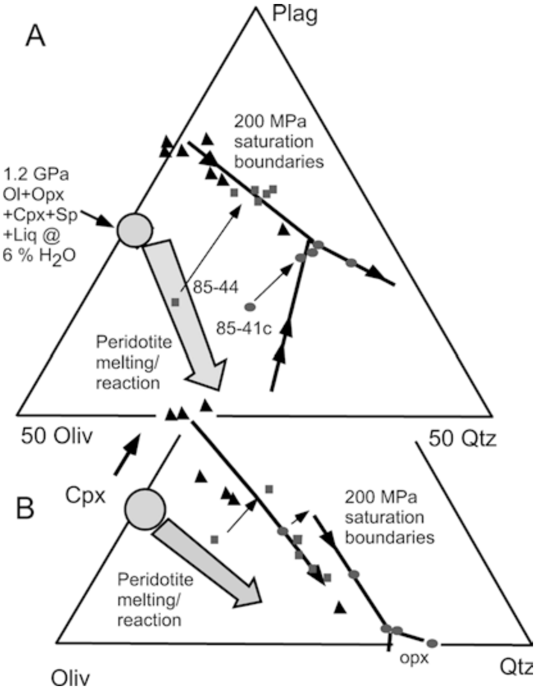

Fig. 8 Compositions of 200-MPa, NNO, H_2O-saturated liquids on the pseudoternary projections: **A** Olivine (Oliv)-Plagioclase (Plag)-Quartz (Qtz) projected from Clinopyroxene (Cpx) showing only the upper half of the triangle from 50% Oliv-50% Qtz to 100% Plag. **B** Oliv-Cpx-Qtz projection scheme from Plag. Projection scheme is from Tormey et al. (1987) and Grove (1993). *Symbols* and saturation boundaries are the same as in Fig. 6. *Thin arrows* pointing away from 85-44 and 85-41c starting compositions indicate fractionation paths. Also shown are the 1.2-GPa, 6 wt% H_2O liquids saturated with ol + opx + cpx + sp from Gaetani and Grove (1998). The oliv + opx melting reaction followed during hydrous mantle melting after cpx + sp are exhausted is shown by the *dark gray arrow* (Table 4) and is defined by crystallization of oliv and melting of opx

calculate this melting reaction (Table 4). The first set of results in Table 4 are least squares mass balance calculations that relate an average of the experimental liquids (MM in Table 4) saturated with oliv + opx + cpx + sp at 1.2-GPa and containing ~6 wt% H_2O. This average liquid is used in the mass balance to calculate the phase assemblage necessary to relate it to liquids saturated with ol + opx + cpx (B392 in Table 4), or ol + opx (B384 and B388 in Table 4). The calculated coefficients are given in Table 4 (1. MBC).

These coefficients are consistent with the melting reaction:

$$1.0\ \mathrm{Opx} = 0.5\ \mathrm{Oliv} + 0.5\ \mathrm{Liq} \qquad (1)$$

In this melting reaction, opx dissolves as oliv + melt are produced. This is the well-known incongruent melting of opx to oliv + liquid that operates at low pressure and/or high magmatic H_2O contents. This reaction leads to significant silica enrichment in the high-extent mantle melts produced after cpx and sp are exhausted as residual phases. The path followed by liquids as melting proceeds has been calculated (Table 4, 2.

PRM) using the Gaetani and Grove multiply saturated melt (MM in Table 4), and the phase proportions from the mass balance from Table 4. The path is plotted in Figs. 7 and 8.

An additional mass balance calculation (Table 4, 3. NLM) was performed using the compositions of 85-44 and 85-41c, the Gaetani and Grove mantle multiply saturated (oliv + opx + cpx + sp) melts and the major element composition (Na_2O + K_2O) of the slab-derived fluid-rich component from Grove et al. (2002) to calculate the melting reaction. The results are shown in Table 4 and require similar proportions of oliv and opx. The major elements (Na_2O + K_2O) in the fluid-rich component that were used in this calculation were assumed to be added at the bottom of the wedge during vapor-saturated melting of peridotite, and they have been significantly diluted during flux melting (see Grove et al. 2002; Gaetani and Grove 2003).

The three different approaches discussed above all point to reaction [1], the incongruent melting of opx on the oliv + opx reaction boundary, as the process responsible for moving primitive subduction zone magmas to the low FeO*/MgO and high SiO_2 portion of the Miyashiro diagram. This reaction operates once cpx + sp are exhausted as mantle residue phases and harzburgite becomes the mantle source rock. In the pseudoternary projections schemes, the influence of opx melting and oliv crystallization is to increase SiO_2 and decrease Al_2O_3, driving the mantle melts first to basaltic andesites like 85-44, and, with further melting, to hypersthene-normative compositions like that of 85-41c (Fig. 8).

An alternative mechanism for producing these SiO_2-rich liquids in the mantle wedge is melt–wall-rock interaction. Kelemen (1990) and Kelemen et al. (1997) propose that melts rising through the mantle will become saturated with oliv and undersaturated in opx as the oliv + opx boundary shifts to higher SiO_2 contents with decreasing pressure. This mode of reaction is identical to reaction [1] and it now results in assimilation of opx with precipitation of oliv, raising the SiO_2 content of a magma without significantly affecting the other major and trace elements. Because the assimilation process is controlled by the same saturation boundaries and crystal-melt reactions that govern melting, it is difficult to distinguish assimilation from a progressive melting and re-equilibration process that takes place at low pressures. However, both processes are restricted to shallow mantle depths and high H_2O contents.

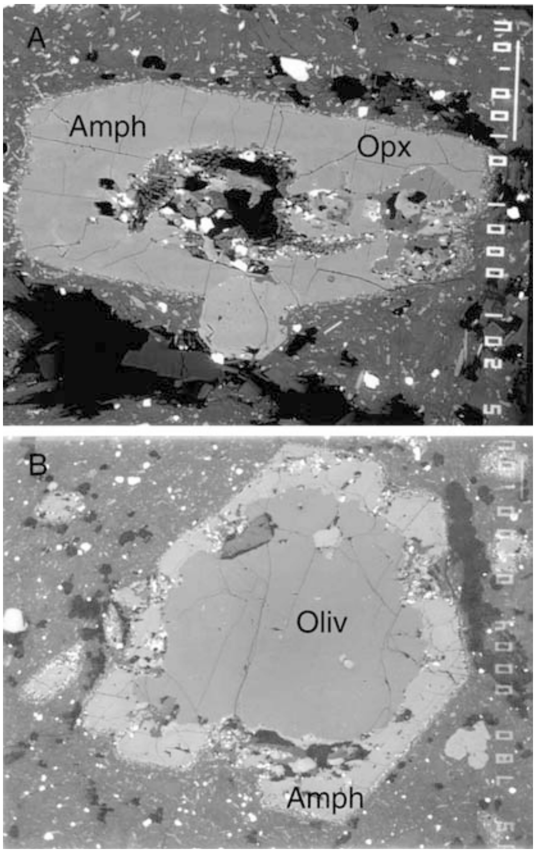

Fig. 9 Amphibole and associated overgrowth minerals from Mt. Shasta andesite 82-85 (Table 5). Backscattered electron images with *scale bars* of 100 μm (*upper right*). **A** Euhedral amphibole exhibiting internal skeletal growth form. On the right side of the crystal is an inclusion of high Mg# opx (Mg# =0.87). **B** Rounded and amoeboid shaped olivine crystal (Fo_{88}) surrounded by high Mg# amphibole

Miyashiro (1974) recognized that there is not a single calc-alkaline or tholeiitic suite, but that a continuum exists from tholeiitic to calc-alkaline, and that each arc has its own distinctive signature. In addition, many arc volcanoes possess both tholeiitic and calc-alkaline suites (e.g., Hakone region, Japan and the Nasu volcanic zone, northeast Japan, Cascades, USA). Miyashiro (1974) also found that many arcs (particularly notable is the largest arc on Earth, the Mariana arc) display FeO*/MgO vs. SiO_2 variations that lie on the tholeiitic side of the plot. The trends defined by Sisson and Grove (1993a), therefore, are characteristic of a large volume of the Earth's current output of arc magmatism, and represent fractional crystallization trends produced by high magmatic H_2O content melts under crustal level conditions. Based on the reasoning presented above, these hydrous fractional crystallization trends are the ones expected to result when the starting point for fractionation is a H_2O-rich mantle melt produced at high pressures and saturated with oliv + opx + cpx + sp or oliv + opx + cpx + garnet. The mantle melt compositions that define the starting point for fractionation from these liquids are represented by the large gray dot in Figs. 7 and 8, and the calc-alkaline fractional crystallization paths followed by these liquids coincide with the TH-CA boundary.

The calc-alkaline differentiation trends delineated by the Shasta region primitive lavas lie in a portion of the diagram that is not as commonly represented by modern arc environments. Similar lavas are found in other hot-slab environments, where young oceanic lithosphere is being subducted. Localities include Shasta, the Adak region of Alaska (Kay 1978; Yogodzinski et al. 1995), the Setouchi belt of SW Japan arc (Ishizaka and Carlson 1983; Tatsumi and Ishizaka 1983; Shimoda et al. 1998),

Table 5 Compositions of minerals in Mt. Shasta magnesian andesites

Sample no.	Mineral	SiO_2	TiO_2	Al_2O_3	Cr_2O_3	FeO	MnO	MgO	CaO	Na_2O	K_2O	P_2O_5	Sum	Mg# or An
82-85														
inc.[a]	Oliv	40.3		0.11		12.8	0.24	48.3	0.22				102.0	0.870
og[a]	Amph	45.4	1.71	10.7	0.25	6.75		18.9	11.64	2.64	0.67		98.6	0.833
inc	Cpx	52.7	0.39	2.15	0.10	6.01	0.24	16.9	20.9	0.31			99.8	0.834
og	Amph	44.8	1.92	11.1	0.46	7.42	0.03	18.1	11.3	2.55	0.62		98.4	0.813
ig[a]	Cpx	52.2	0.47	3.42	0.31	5.91	0.17	16.8	21.2	0.56			101.1	0.835
ig	Plag	56.6		27.5		0.25		0.02	9.84	6.13	0.24		100.5	0.463
82-88a														
inc	Oliv	39.7		0.03		17.8	0.25	44.2			0.33		102.0	0.815
og	Amph	45.1	1.47	11.5		9.55	0.21	17.7	11.4	2.51			99.9	0.768
85-59														
inc	Oliv	40.1		0.03	0.04	16.7	0.21	44.0	0.11				101.7	0.823
inc	Opx	55.9	0.13	1.19	0.03	12.0	0.30	30.4	1.32	0.02			101.3	0.818
og	Amph	43.8	2.10	11.8	0.02	8.40	0.10	17.0	11.6	2.37	0.53		97.7	0.782
pheno	Plag	56.4		27.6		0.27			10.5	5.43	0.19		100.4	
ig	Usp-mag	0.12	6.05	1.73	0.30	83.8	0.38	2.24					94.7	
ig	Ilm-hem	0.07	30.5	0.33	0.14	62.8	0.38	3.31					97.6	
83-56														
inc	Opx	55.2	0.14	2.09	0.14	11.3	0.24	31.3	1.13				101.5	0.813
og	Amph	46.6	1.55	10.5	0.04	7.88	0.12	17.7	11.3	2.12	0.24		98.1	0.800
96-5														
inc	Opx	55.3	0.17	1.34	0.45	9.58	0.23	30.3	1.13	0.04			98.5	0.849
inc	Cpx	53.2	0.19	1.79	0.21	5.62	0.22	16.2	21.5	0.32			99.2	0.837
og	Amph	46.6	1.08	9.44	0.41	7.80	0.11	17.6	11.2	2.95	0.18		97.3	0.800
96-11b														
inc	Cpx	53.0	0.17	1.74	0.75	4.16	0.14	16.7	22.0	0.29			99.0	0.878
og	Amph	47.0	1.05	9.10	0.38	7.18	0.08	17.4	11.4	2.51	0.20		96.3	0.812
97-1f														
inc	Oliv	39.8		0.01	0.02	13.8	0.16	45.2	0.11				99.1	0.854
inc	Cpx	53.1	0.30	2.04	0.70	4.64	0.07	16.9	21.1	0.38			99.3	0.866
og	Amph	45.5	2.12	10.7	0.09	7.90	0.14	17.4	11.3	2.48	0.52		98.2	0.797
Melt inclusion 246-4-1 in opx, S76 of (Anderson 1979)														H_2O[b]
		61.1	0.32	16.8	0.09	0.71	0.15	0.38	3.42	3.02	1.65	0.21	99.82	10.7
Lavas[c]														Mg#
82-85	SR	61.46	0.66	16.99		4.58		3.83	5.87	4.40	1.82	0.30		0.598
82-88a	SR	63.53	0.59	16.89		4.02		2.81	5.16	4.69	1.95	0.28		0.555
85-59	SR	60.29	0.73	16.78		4.86		4.34	6.14	4.60	1.84	0.34		0.614
83-56	M	65.62	0.44	16.64		2.94		2.16	4.86	4.60	1.36	0.12		0.567
96-5	SH	64.36	0.49	16.89		3.47		3.47	6.07	4.07	0.99	0.13		0.641
96-11b	SH	64.90	0.51	16.99		3.41		3.02	5.96	3.90	1.08	0.15		0.612
97-1f	SR	57.64	0.92	16.84		5.57		5.11	7.31	4.23	1.81	0.48		0.621
S76	SH	63.62	0.60	16.71		3.86		3.55	6.08	4.16	1.15	0.21		0.621

[a] *inc*. Inclusion in mineral; *og* overgrowing mineral; *ig* intergrowth

[b] Melt inclusion in opx (Mg# 0.84–0.89, Anderson 1979) in Shastina andesite S76. Resampled as 97-7 by TL Grove; H_2O estimated from quantitative analysis of oxygen by electron microprobe (see Gaetani and Grove 1998)

[c] Mt. Shasta region lavas. *SR* Sargents Ridge; *M* Misery; *SH* Shastina. These are eruptive stages of the Mt. Shasta stratocone. See Christiansen et al. (1977)

the Mexican Volcanic Belt (Blatter and Carmichael 2001), and the Chilean arc (Stern and Kilian 1996). These lavas plot in the low FeO*/MgO and high SiO_2 portion of Fig. 5 because they represent high degree melts of refractory mantle with only oliv + opx as residual phases (Fig. 4). The increased extent of hydrous mantle melting at shallow mantle depths has produced SiO_2-rich primitive parent melts with low FeO at elevated MgO contents (Figs. 7 and 8).

Evidence for high water contents in primitive Mt. Shasta region magmas

The petrologic evidence preserved in the primitive Mt. Shasta region lavas is suggestive of pre-eruptive H_2O contents of 4.5 to 6.5 wt%. These values are significantly higher than those inferred by early experimental studies of the influence of H_2O on mantle melting (e.g., Kushiro 1968, 1969, 1972). These studies argued that thermodynamic effects of H_2O on melt composition produced the high SiO_2 by addition of only 2 to 3 wt% H_2O to the melt.

There is petrologic evidence in Mt. Shasta lavas suggestive of even higher pre-eruptive H_2O contents. The evidence is found in several high-Mg# andesite and dacite lavas of the Mt. Shasta stratocone. These lavas preserve petrologic signatures that indicate complex mixing processes between primitive and evolved melt components. These mixed lavas may record a fractionation event that occurred in a primitive magnesian andesite under high pressure (~800 MPa) and high H_2O contents (> 10 wt%). In some lavas, a magnesian pargasitic amph is preserved in overgrowth relation with magnesian oliv, opx, and cpx (Fig. 9, Table 5). This magnesian pargasite is similar in composition to the amph produced in the 800-MPa, H_2O-saturated experiments on 85-44 (Table 3). As P_{H2O} increases along an oxygen buffer curve (NNO in our experiments), amph appears earlier in the crystallization assemblage until, at 800 MPa, it appears after oliv along with opx and cpx at 1,070 °C. In contrast, amph is the last phase to crystallize in the 200-MPa experiments, appearing by 980 °C. This change in the appearance temperature of amph manifests itself in a systematic variation in Mg# of the amph. This variation is illustrated in Fig. 10, along with experimental data of Blatter and Carmichael (1998) and Moore and Carmichael (1998), who worked on compositions from the Mexican Volcanic Belt at pressures up to 300 MPa and at higher f_{O2} conditions. The Blatter and Carmichael (1998) experiments were performed at NNO + 3 over the pressure range of 150 to 300 MPa, and the Moore and Carmichael (1998) experiments were performed at f_{O2} values between NNO + 1 and NNO + 2. The experiments on the Mexican Volcanic Belt lavas show the important additional influence of variations in f_{O2} on amph appearance. Increasing f_{O2} increases the appearance temperature of amph by decreasing the amount of Fe^{2+} in the melt, thereby increasing liquid Mg#.

A line has been extended between the two 85-44 experimental data at 200 and 800 MPa (Fig. 10). The line approximates the effect of increasing H_2O content at vapor-saturated conditions along the NNO buffer curve on the composition of the first-appearing amph. Also shown are amph compositions from the Shasta lavas. Amphibole is often found in Mt. Shasta andesites (Baker 1988), but it most commonly occurs intergrown with plag. When associated with plag the amph has an Mg# of 0.75 or lower, and the amph crystal overgrows and encloses the plag. The coincidence of Mg# < 0.75 and included plag is consistent with crystallization of andesite liquid at 200 MPa at NNO and H_2O contents of ~6 wt%. The magnesian pargasite assemblages tabulated in Table 5 do not occur with plag, but exist in an overgrowth relation with magnesian oliv, opx, and/or cpx. This association is consistent with the phase relations (Fig. 2) that show amph appearing as a crystallizing phase with oliv, opx, and cpx before plag at pressures > 400 MPa. The magnesian pargasite assemblages in Shasta andesites are positioned on Fig. 10 according to their Mg#. If this Mg# is used to indicate P_{H2O} of crystallization, values of 500 to > 800 MPa are obtained. The magnesian pargasite amph from 96-5 and 97-1f resemble the amph produced at 800 MPa H_2O-saturated at NNO and one would infer H_2O contents of ~14 wt% (Hamilton et al. 1964) to stabilize this assemblage at NNO. The highest Mg# amph found in the Shasta lavas (82–85) would require H_2O-saturated crystallization at pressures of > 1 GPa, indicating H_2O contents of > 16 wt%, if the simplified extrapolation of Mg# vs. pressure applies.

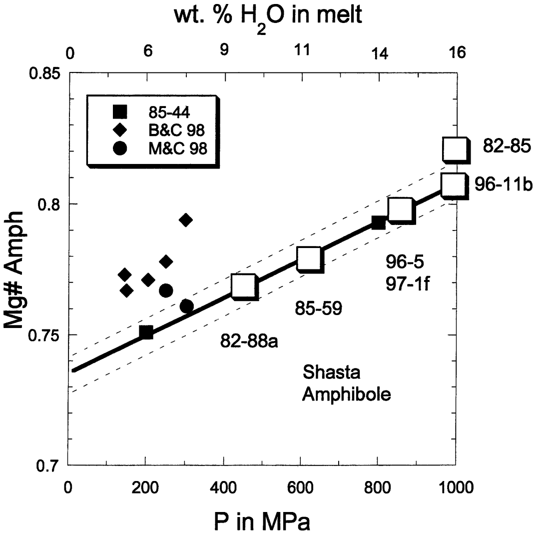

Fig. 10 Mg# of first amphibole to appear in H_2O-saturated experiments on 85-44 at the NNO buffer at 200 and 800 MPa is plotted against pressure (*solid squares*). *Dark line* was placed through these two amphibole compositions and assumes a linear relation between pressure and Mg# of amphibole, as amphibole appears as an earlier phase in the crystallizing assemblage (Fig. 2). *Upper scale* shows H_2O contents of H_2O-saturated liquids using the method of Hamilton et al. (1964). Also shown are experiments performed by Blatter and Carmichael (1998) on a high-SiO_2 andesite at NNO + 3 and from Moore and Carmichael (1998) at NNO + 1 and NNO + 2. Crystallization conditions for Shasta lavas is inferred to be NNO + 1.8 or lower. *Large open squares* are compositions of high Mg# amphiboles that contain included opx, cpx, or oliv (Table 5). Plot has not been extended to pressures greater than 1 GPa. The high Mg# of 82–85 would indicate higher pressure, but we are not confident of this extrapolation. *Dashed boundary* on either side of the Mg#–P line is the 2σ uncertainty of amphibole composition from replicate analyses reported in Table 3

Additional support for high pre-eruptive H_2O contents comes from the H_2O content of melt inclusions in Mt. Shasta primitive lavas. Anderson (1979) estimated ~13 wt% H_2O in melt inclusions in opx (Mg# = 0.84–0.89) in Shastina lavas. We reanalyzed these melt inclusions quantitatively for oxygen and obtained H_2O contents of 10.5 to 10.7 wt% (Table 5, 246-4-1).

Oxygen fugacity variations are an additional important variable in controlling amphibole composition. Also present in the andesites are coexisting usp and ilmenite (Table 5, 85-59). The QUILF barometer of Andersen and Lindsley (1988) was applied to this assemblage to estimate temperature and f_{O2}. An f_{O2} value of NNO + 1.8 at 890 °C is obtained from the coexisting oxides, and this assemblage crystallized in the evolved rhyodacite liquid that constitutes one mixing end member in the Shasta andesite. If this value of f_{O2} was also relevant for the crystallization of the magnesian end member in the mixed lava, it would lower the pressure of crystallization inferred from the NNO experimental data by ~150 MPa, and the maximum pre-eruptive H_2O content would be ~14 wt%.

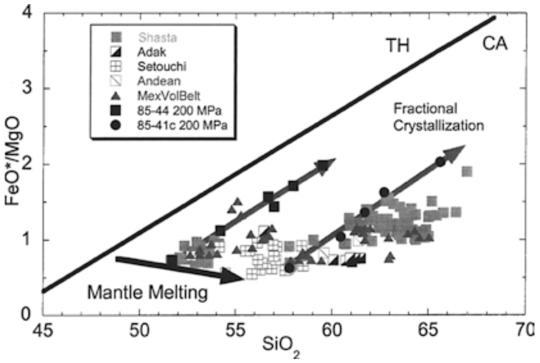

Fig. 11 Compositions of selected suites of high-Mg, high-SiO_2 lavas plotted on the FeO*/MgO vs. SiO_2 diagram. The tholeiitic (TH)–calc-alkaline (CA) dividing line is from Miyashiro (1974). *Symbols* (*black*) and *lines* (*dark gray*) for 85-44 and 85-41 show crystallization paths followed under 200 MPa H_2O-saturated conditions at NNO. *Solid black line labeled mantle melting* is the path followed by mantle melts generated by melting of harzburgite. The *left-hand-side of the line* begins where cpx + sp are exhausted from the mantle residue at ˜20% melting at 1.2 GPa (Gaetani and Grove 1998). At the *right-hand arrow*, an additional 20% melting of oliv + opx has occurred. Also shown are lavas from the Mt. Shasta region (Baker 1988; Baker et al. 1994; Grove et al. 2002),the Adak Island region of Alaska (Kay 1978; Yogodzinski et al. 1995), the Setouchi volcanic belt (Tatsumi and Ishizaka 1982; Shimoda et al. 1998), the Andean Austral Volcanic Zone (Stern and Killian 1996) and the Mexican Volcanic Belt (Luhr and Carmichael 1985; Carmichael et al. 1996; Blatter and Carmichael 2001)

With the realization that amph composition may be a complex indicator of pre-eruptive H_2O content and f_{O2} variations, we present these results with caution. However, the amphibole and melt inclusion data are consistent with the existence of Mt. Shasta lavas that contain pre-eruptive H_2O contents >10 wt% H_2O. The magnesian amph assemblages are present in $\sim$10% of the andesite and dacite lavas that have been sampled at Mt. Shasta. They are represented in three (Sargents, Misery and Shastina) of the four Shasta eruptive units described by Christiansen et al. (1977). High-Mg amph are present in greatest abundance in the Shastina lavas, where nearly every dacite sampled contains the assemblage magnesian amph enclosing opx, cpx, and/or oliv. The opx containing melt inclusions with 10.7 wt% H_2O is also from a Shastina dacite (S76, Anderson 1979).

Role of fractional crystallization in the generation of Adakites, Setouchi andesites, and Archean TTG suites.

A number of subduction zone lavas exhibit trace element geochemical signatures that are consistent with a significant trace element contribution from the subducted oceanic lithosphere. These include the Adak-type high-Mg andesites from the Aleutians (Kay 1978; Yogodzinski et al. 1995), the Setouchi high-Mg andesites from SW Japan (Tatsumi and Ishizaka 1982; Ishizaka and Carlson 1983; Shimoda et al. 1998), the andesites of the Mexican Volcanic Belt (Luhr and Carmichael 1985; Carmichael et al. 1996), and high-Mg andesites from Cook Island in the Andean Austral volcanic zone (Stern and Kilian 1996). These lavas are shown in Fig. 11 on the Miyashiro (1974) FeO*/MgO vs. SiO_2 plot along with the compositions of Mt. Shasta primitive lavas and stratocone andesites and dacites. There are striking similarities between the Mt. Shasta region andesites and these other high-SiO_2, high-MgO lavas. The primitive end members of the Setouchi lavas are quite similar to both the primitive basaltic andesite and magnesian andesites from the Mt. Shasta region, and high-pressure experiments by Tatsumi (1982) and Tatsumi et al. (1983) indicate a mantle origin and high H_2O contents under conditions similar to those inferred for the Shasta lavas. Petrologic studies (Tatsumi and Ishizaka 1982) show mineral assemblages that are consistent with equilibration with a refractory mantle residue assemblage. High Mg# oliv (Stern and Kilian 1996) and cpx (Yogodzinski and Kelemen 1998) are also found in the Adak high-Mg lavas. Petrologic and experimental studies of the Mexican Volcanic Belt lavas (Blatter and Carmichael 1998; Moore and Carmichael 1998) indicate pre-eruptive H_2O contents of at least 6 wt% and Luhr and Carmichael (1985) identify primitive parent magmas.

In these lavas there are strong trace element and isotopic contributions inherited from subducted lithosphere (basalt and sediment). Adak andesite lavas show strong MORB trace element and isotopic signatures and Setouchi andesite lavas contain a strong sediment signature. The Shasta region primitive lavas preserve both sediment-derived and MORB-derived trace element and isotopic signatures (Grove et al. 2002). However, the additional inference is often made that the major element characteristics of these lavas are produced by direct melting of the subducted slab (Defant and Drummond 1990). This reasoning has been extended to Archean times where SiO_2-rich plutonic rocks, the trondhjemite–-tonalite–-granodiorite suite (TTG suite) are found to possess similar major and trace element characteristics (Martin 1987; Smithies 2000).

We propose an alternative to a single-stage slab-melting model that attempts to explain both major and trace element characteristics of these lavas. The major element characteristics of these magmas are inherited from a flux melting process that began at the base of the mantle wedge, and extended through the wedge. The result is a high-SiO_2, high-MgO, high-H_2O melt saturated with harzburgite at shallow mantle depth. Subsequent fractional crystallization under hydrous conditions produced SiO_2-rich derivative liquids that follow calc-alkaline differentiation trends. This melting was fluxed by an H_2O-rich and trace element-rich fluid component released by dehydration of the subducting ocean lithosphere (Grove et al. 2002). The trace element inventory is contributed by the H_2O-rich component. The major element composition is determined by the temperature–-depth structure in the wedge. The mantle melting process is the incongruent melting of opx to oliv + melt. This process can only occur at shallow depths. Thus, the high-SiO_2 signature of these lavas indicates shallow mantle melting under hydrous conditions.

Conclusions

This paper has discussed the influence of H_2O in controlling the mantle melting and fractional crystallization of primitive, high-SiO_2, subduction-related lavas. Pre-eruptive H_2O contents of 4.5 to 6 wt% are present in these lavas, but some lavas may contain higher magmatic H_2O as high as 10 wt% H_2O. These high H_2O contents, combined with high extents of shallow mantle melt reaction, may be the critical ingredients that lead to the production of the rare, but important low-FeO*/MgO, high-SiO_2 primitive arc magmas. Thus, primitive high-SiO_2 lavas from young hot-slab subduction zones are characterized by high extents of mantle melting at high magmatic H_2O contents.

Acknowledgements The authors thank J. Gill and J. Longhi for thoughtful reviews. This research was supported by National Science Foundation Grants EAR-9706214, EAR-0073766, and OCE-00001821. T.L.G. thanks A.N. Halliday and ETH, Zurich, for providing support as a Gastdozent during the preparation of this manuscript.

References

Albee AL, Ray L (1970) Correction factors for electron probe microanalysis of silicates, oxides, carbonates, phosphates and sulfates. Anal Chem 42:1408–1414

Anderson AT (1974) Evidence for a picritic, volatile-rich magma beneath Mt. Shasta, California. J Petrol 15:243–267

Anderson AT (1979) Water in some hypersthenic magmas. J Geol 87:509–531

Andersen DJ, Lindsley DH (1988) Internally consistent solution model for Fe–Mg–Mn oxides: Fe–Ti oxides. Am Mineral 73:714–726

Armstrong JT (1995) CITZAF—a package of correction programs for the quantitative electron microbeam X-ray analysis of thick polished materials, thin-films and particles. Microbeam Anal 4:177–200

Baker MB (1988) Evolution of lavas at Mt. Shasta volcano, N California: an experimental and petrologic study. PhD Thesis, MIT, Massachusetts

Baker MB, Grove TL, Price R (1994) Primitive basalts and andesites from the Mt. Shasta region, N California: products of varying melt fraction and water content. Contrib Mineral Petrol 118:111–129

Bence AE, Albee AL (1968) Empirical correction factors for the electron microanalysis of silicates and oxides. J Geol 76:382–403

Blatter DL, Carmichael ISE (1998) Plagioclase-free andesites from Zitacuaro (Michoacan), Mexico: petrology and experimental constraints. Contrib Mineral Petrol 132:121–138

Blatter DL, Carmichael ISE (2001) Hydrous phase equilibria of a Mexican high-silica andesite: a candidate for mantle origin? Geochim Cosmochim Acta 65:4043–4065

Boyd FR, England JL (1960) Apparatus for phase equilibrium studies at pressures up to 50 kilobars and temperatures up to 1,750 °C. J Geophys Res 65:741–748

Bryan WB, Finger LW, Chayes F (1969) Estimating proportions in petrographic mixing equations by least squares approximation. Science 163:926–927

Carmichael ISE, Lange RA, Luhr JF (1996) Quaternary minettes and associated volcanic rocks of Mascota, western Mexico: a consequence of plate extension above a subduction modified mantle wedge. Contrib Mineral Petrol 124:302–333

Christiansen RL, Kleinhampl FJ, Blakely RJ, Tuchek ET, Johnson FL, Conyac MD (1977) Resource appraisal of the Mt. Shasta wilderness study area, Siskiyou County, California. Open-file report 77-250, US Geol Surv, 538

Defant MJ, Drummond MS (1990) Derivation of some modern arc magmas by melting of young subducted lithosphere. Nature 347:662–665

Fuis GS, Zucca JJ, Mooney WD, Milkereit B (1987) A geologic interpretation of seismic-reflection results in northern California. Geol Soc Am Bull 98:53–65

Gaetani GA, Grove TL (1998) The influence of water on melting of mantle peridotite. Contrib Mineral Petrol 131:323–346

Gaetani GA, Grove TL (2003) Experimental constraints on melt generation in the mantle wedge. In: Eiler J, Abers G (eds) The subduction factory. Am Geophysical Union, Washington, DC (in press)

Gaetani GA, Grove TL, Bryan WB (1994) Experimental phase relations of basaltic andesite from Hole 839B under hydrous and anhydrous conditions. Proc Ocean Drill Program Sci Results 135:557–563

Gill JB (1981) Orogenic andesites and plate tectonics. Springer, Berlin Heidelberg New York

Green NL, Harry DL (1999) On the relationship between subducted slab age and arc basalt petrogenesis, Cascadia subduction system, North America. Earth Planet Sci Lett 171:367–381

Grove TL (1981) Use of FePt alloys to eliminate the iron loss problem in 1-atmosphere gas mixing experiments: theoretical and practical considerations Contrib Mineral Petrol 78:298–304

Grove TL (1993) Corrections to expressions for calculating mineral components. In: Origin of calc-alkaline series lavas at Medicine Lake Volcano by fractionation, assimilation and mixing and experimental petrology of normal MORB near the Kane fracture zone:22°–25°N, mid-Atlantic ridge. Contrib Mineral Petrol 114:422–424

Grove TL, Baker MB (1984) Phase equilibrium controls on the calc-alkaline vs. tholeiitic differentiation trends. J Geophys Res 89:3253–3274

Grove TL, Bence AE (1977) Experimental study of pyroxene–liquid interaction in quartz-normative basalt 15597. Proc Lunar Sci Conf 8:1549–1579

Grove TL, Juster TC (1989) Experimental investigations of low-Ca pyroxene stability and olivine–pyroxene–liquid equilibria at 1-atm in natural basaltic and andesitic liquids. Contrib Mineral Petrol 103:287–305

Grove TL, Kinzler RJ (1986) Petrogenesis of andesites. Annu Rev Earth Planet Sci 14:417–454

Grove TL, Donnelly-Nolan JM, Housh T (1997) Magmatic processes that generated the rhyolite of Glass Mountain, Medicine Lake volcano, N California. Contrib Mineral Petrol 127:205–223

Grove TL, Parman SW, Bowring SA, Price RC, Baker MB (2002) The role of an H_2O-rich fluid component in the generation of primitive basaltic andesites and andesites from the Mt. Shasta region, N California. Contrib Mineral Petrol 142:375–396

Hamilton DL, Burnham CW, Osborn EF (1964) The solubility of water and the effects of oxygen fugacity and water content on crystallization in mafic magmas. J Petrol 5:21–39

Hays JF (1966) Lime-alumina-silica. Carnegie Inst Washington Yearbook 65:234–239

Hirose K (1997) Melting experiments on lherzolite KLB-1 under hydrous conditions and the generation of high-magnesian andesitic melts. Geology 25:42–44

Hirose K, Kawamoto T (1995) Hydrous partial melting of lherzolite at 1 GPa: the effect of H_2O on the genesis of basaltic magmas. Earth Planet Sci Lett 133:463–473

Holloway JR, Burnham CW (1972) Melting relations of basalt with equilibrium water pressures less than total pressure. J Petrol 13:1–29

Ishizaka K, Carlson RW (1983) Nd–Sr systematics of the Setouchi volcanic rocks, southwest Japan: a clue to the origin of orogenic andesite. Earth Planet Sci Lett 64:327–340

Juster TC, Grove TL, Perfit MJ (1989) Experimental constraints on the generation of FeTi basalts, andesites and rhyodacites at the Galapagos Spreading Center, 85°W and 95°W. J Geophys Res 94:9251–9274

Kay RW (1978) Aleutian magnesian andesites: melts from subducted Pacific ocean crust. J Volcanol Geotherm Res 4:117–132

Kelemen PB (1990) Reaction between ultramafic rock and fractionating basaltic magma I. Phase relations, the origin of calc-alkaline magma series, and the formation of discordant dunite. J Petrol 31:51–98

Kelemen PB, Hirth JG, Shimizu N, Spiegelman M, Dick HBJ (1997) A review of melt migration processes in the adiabatically upwelling mantle beneath oceanic spreading ridges. Phil Trans R Soc Lond 355:283–318

Kinzler RJ, Donnelly-Nolan JM, Grove TL (2000) Late Holocene hydrous mafic magmatism at the Paint Pot Crater and Callahan Flows, Medicine Lake Volcano, N California and the influence of H_2O in the generation of silicic magmas. Contrib Mineral Petrol 138:1–16

Kushiro I (1968) Compositions of magmas formed by partial melting of the Earth's upper mantle. J Geophys Res 73:619–634

Kushiro I (1969) The system forsterite–diopside–silica with and without water at high pressures. Am J Sci 267A:269–294

Kushiro I (1972) Effect of water on the compositions of magmas formed at high pressures. J Petrol 13:311–334

Kushiro I (1990) Partial melting of mantle wedge and evolution of island arc crust. J Geophys Res 95:15929–15939

Longhi J (1991) Comparative liquidus equilibria of hypersthene–normative basalts at low pressure. Am Mineral 76:785–800

Luhr JF, Carmichael ISE (1985) Jorullo Volcano, Michoacan, Mexico (1759–1774): the earliest stages of fractionation in calc-alkaline magmas. Contrib Mineral Petrol 90:142–161

Martin H (1987) Petrogenesis of Archean trondhjemites, tonalite and granodiorites from eastern Finland—major and trace element geochemistry. J Petrol 28:921–953

Miyashiro A (1974) Volcanic rock series in island arc and active continental margins. Am J Sci 274:321–355

Moore G, Carmichael ISE (1998) The hydrous phase equilibria (to 3 kbar) of an andesite and basaltic andesite from western Mexico: constraints on water content and conditions of phenocryst growth. Contrib Mineral Petrol 130:304–319

Müntener O, Kelemen PB, Grove TL (2001) The role of H_2O during crystallization of primitive arc magmas under uppermost mantle conditions and genesis of igneous pyroxenites: an experimental study. Contrib Mineral Petrol 141:643–658

Shimoda G, Tatsumi Y, Nodha S, Ishizaka K, Jahn BM (1998) Setouchi high-Mg andesites revisited: geochemical evidence for melting of subducted sediments. Earth Planet Sci Lett 160:479–492

Sisson TW, Grove TL (1993a) Experimental investigations of the role of water in calc-alkaline differentiation and subduction zone magmatism. Contrib Mineral Petrol 113:143–166

Sisson TW, Grove TL (1993b) Temperature and H_2O contents of low-MgO high-alumina basalts. Contrib Mineral Petrol 113:167–184

Sisson TW, Layne GD (1993) H_2O in basalt and basaltic and andesite glass inclusions from four subduction-related volcanoes. Earth Planet Sci Lett 117:619–635

Smithies RB (2000) The Archean tonalite–trondhjemite–granodiorite (TTG) series is not an analogue of Cenozoic adakite. Earth Planet Sci Lett 182:115–125

Stern CR, Kilian R (1996) Role of subducted slab, mantle wedge and continental crust in the generation of adakites from the Andean Austral Volcanic Zone. Contrib Mineral Petrol 123:263–281

Tatsumi Y (1982) Origin of high-magnesian andesites in the Setouchi volcanic belt, southwest Japan, II. Melting phase relations at high pressures. Earth Planet Sci Lett 60:305–317

Tatsumi Y, Ishizaka K (1982) Origin of high-magnesian andesites in the Setouchi volcanic belt, southwest Japan, I. Petrographical and chemical characteristics. Earth Planet Sci Lett 60:293–304

Tatsumi Y, Sakuyama M, Fukuyama H, Kushiro I (1983) Generation of arc basalt magmas and thermal structure of the mantle wedge in subduction zones. Geophys Res 88:5815–5825

Thorpe RS (1982) Andesites: orogenic andesites and related rocks. Wiley, New York

Tormey DL, Grove TL, Bryan WB (1987) Experimental petrology of normal MORB near the Kane Fracture Zone: 22°–25°N, mid-Atlantic ridge. Contrib Mineral Petrol 96:121–139

Wagner TP, Donnelly-Nolan JM, Grove TL (1995) Evidence of hydrous differentiation and crystal accumulation in the low-MgO, high-Al_2O_3 Lake Basalt from Medicine Lake volcano, California. Contrib Mineral Petrol 121:201–216

Wilson D (1988) Tectonic history of the Juan de Fuca ridge over the last 40 million years. J Geophys Res 93:11863–11876

Yogodzinski GM, Kelemen PB (1998) Slab melting in the Aleutians: implications of an ion probe study of clinopyroxene in primitive adakite and basalt. Earth Planet Sci Lett 158:53–65

Yogodzinski GM, Kay RW, Volynets ON, Koloskov AV, Kay SM (1995) Magnesian andesite in the western Aleutian Komandorsky region: implications for slab melting and processes in the mantle wedge. Geol Soc Am Bull 107:505–519

Zhang Y-G, Frantz JD (2000) Enstatite–forsterite–water equilibria at elevated temperatures and pressures. Am Mineral 85:918–925